

Vortex-nucleus interaction in the inner crust of neutron stars

P. Avogadro^{1,2}, F. Barranco³, R.A. Broglia^{1,2,4}, and E. Vigezzi²

¹Department of Physics, University of Milan, Via Celoria 16, 20133, Milan, Italy

²INFN, Sezione di Milano, Milan, Italy

³Escuela Tecnica Superior de Ingenieros, Universidad de Sevilla,
41092 Camino de los Descubrimientos s/n, Sevilla, Spain

⁴The Niels Bohr Institute, University of Copenhagen,
Blegdamsvej 17, 2100 Copenhagen, Denmark

Abstract

The structure of a vortex in the inner crust of neutron stars is calculated within the framework of quantum mean field theory taking into account the interaction with the nuclei composing the Coulomb lattice. Making use of the results obtained with different nuclear interactions, the pinning energy, relevant in the study of glitches, is worked out. Quantal size and density dependent effects are found to be important.

I. INTRODUCTION

According to standard theoretical models, the inner crust of a neutron star, where a lattice of nuclei is surrounded by a sea of free neutrons and relativistic electrons, lies in the range of densities between 4×10^{11} and 1.6×10^{14} g/cm³ ($0.0014 n_0$ and $0.57 n_0$, where n_0 is the nuclear saturation density, $n_0 = 0.16 \text{ fm}^{-3} = 2.8 \times 10^{14} \text{ g/cm}^3$). The first microscopic study of this system was carried out by Negele and Vautherin. They determined, making use of a Skyrme-like functional of the energy, the isotopic composition as well as the distance between the (spherical) nuclei forming the Coulomb lattice [1]. Subsequent studies found that for densities larger than about $n_0/3$, other shapes rather than spherical become favoured [2]-[4]. This is still a debated topic. In any case, in our study we shall limit ourselves to densities $n < n_0/3$, where the assumption of spherical nuclei is considered to be safe. Another assumption at the basis of Negele and Vautherin's study was the Wigner-Seitz approximation, in which one studies a single cell of the lattice. Only very recently calculations using band theory have been performed [5].

Studies of neutron matter testify to the fact that the system is superfluid in a wide range of densities [6]. This result implies that the rotation of the star leads to the formation of vortices in the crust. They are expected to form an array whose average density per unit area is given by the Onsager-Feynman formula:

$$\rho = 4m\frac{\Omega}{\hbar}, \quad (1)$$

where Ω is the angular velocity of the star and m is the nucleon mass. The above relation leads to an average (macroscopic) distance between vortices of the order of 10^{-3} cm for $\Omega \sim 1 \text{ ms}^{-1}$.

The presence of impurities - represented, in the present case, by the nuclei constituting the lattice - has a profound influence on pairing correlations and on vortex dynamics. In fact, momentum is much higher inside the nuclear volume than in the surrounding neutron sea. This fact leads, as a rule, to a decrease of the pairing gap. Vortices, whose core is made out of normal matter, may thus find it energetically favourable to pin to the impurities, reducing the loss of pairing energy.

One of the reasons for the interest in the interaction between vortex and nuclei in the inner crust is due to its relation with a possible explanation for the phenomenon of glitches, the sudden spinup of the rotation frequency observed in many neutron stars [7, 8].

Considerable information concerning glitches has been accumulated over the years, and their properties are compatible with the inner crust as their origin [9]. However, a detailed comparison between observations and theoretical models has never been attempted. This is partly due to the fact that even the basic static interaction between a single nucleus and a vortex has never been studied in detail with state-of-the-art microscopic theory, let alone the much more complex issue of vortex dynamics in the inner crust. Only semiclassical estimates of the pinning energy - the energy cost to build up a vortex on a nucleus, rather than far from it - have been available [10, 11, 12], while the first quantal study of a vortex in uniform neutron matter was worked out only a few years ago [13].

In the following we present a detailed account of a microscopic study, based on Hartree-Fock-Bogoliubov (HFB) quantum mean field theory, of the structure of a vortex in the inner crust of a neutron star (partial accounts of this work were published in refs. [14, 15, 16]). In the present paper we aim at clarifying some basic qualitative features of the nucleus-vortex interaction, which, to our knowledge, have not been considered until now (in particular quantal finite size effects) and are absent from semiclassical models. We are well aware that our work represents only a starting point for a comprehensive understanding of vortices in the inner crust of neutron stars and of their possible relation to the phenomenon of glitches, because of various limitations which remain at the basis of our approach. In particular:

- We treat pairing only at the mean field level. It is well known that medium polarization effects have a deep influence on pairing correlations in homogeneous matter [6]. This is even more so in the case of the inhomogeneous systems associated with each of the Wigner-Seitz cells studied by Negele and Vautherin [17].

- We restrict ourselves to the region of spherical nuclei, while the largest contribution to the moment of inertia of the inner crust come from the deepest layers, where the assumption of spherical nuclei breaks down, and other phases (like the pasta phase) become important.

- We consider the interaction between a single nucleus and the vortex, neglecting the influence of other nuclei building the Coulomb lattice. The soundness of this approximation depends on the vortex radius - becoming unacceptable when the vortex radius is of the order, or larger than, the radius of the Wigner-Seitz cell.

- We assume axial symmetry for the nucleus-vortex system. As a consequence we can only consider special spatial configurations, and we are not able to calculate the pinning energy as a function of the distance between the center of the nucleus and the vortex axis.

- In our calculations we assume a simple isotopic composition for the nuclei, using always the same number of protons $Z = 40$, corresponding to a proton shell closure, as we neglect the spin-orbit term in the single-particle potential. A better calculation should consider the spin-orbit term of the mean field and use an updated version of the original Negele and Vautherin analysis [18], in which the effects of pairing correlations are considered in determining the favoured number of protons and the lattice step, as a function of density.

Finally, there are limitations which are intrinsic to the present status of the theory of nuclear interactions and nuclear structure, in particular concerning the choice of the effective interaction used to produce the mean field. In fact, we shall see that some of our results depend, sometimes even qualitatively, on particular features of the selected nuclear interaction.

II. HARTREE-FOCK-BOGOLIUBOV EQUATIONS

We want to study the properties of nuclei embedded in a sea of superfluid free neutrons, as well as the properties of particular excitations of such a system, namely vortices. The best available tool to carry out such a study at the mean field level is provided by the Hartree-Fock-Bogoliubov (HFB) theory. The associated equations are widely used in both nuclear and solid state physics, where they are better known as the Bogoliubov-De Gennes equations [19, 20]. The HFB equations allow, starting from two-body forces V_{ph} and V_{pair} (assumed to be of zero range) in the particle-hole channel and in the particle-particle channel respectively, to determine in a self-consistent way the single-particle Hartree-Fock Hamiltonian $H = T + U^{HF}$ and the pairing field $\Delta(\mathbf{x})$, as well as the amplitudes u_i, v_i and the energies E_i of the quasi particles. For a given particle species (neutrons or protons), the HFB equations can be written as

$$\begin{cases} (H(\mathbf{x}) - \lambda)u_i(\mathbf{x}) + \Delta(\mathbf{x})v_i(\mathbf{x}) = E_i u_i(\mathbf{x}) \\ \Delta^*(\mathbf{x})u_i(\mathbf{x}) - (H(\mathbf{x}) - \lambda)v_i(\mathbf{x}) = E_i v_i(\mathbf{x}) \end{cases} \quad (2)$$

where λ denotes the chemical potential, which is fixed so as to yield the desired average number of particles.

While this framework is quite solid, the situation is very different concerning the choice of residual interactions acting in the particle-hole and in the particle-particle channel. The situation is made particularly trying, because in the Wigner-Seitz cell we must deal both

with strongly asymmetric matter (in the interior of the nuclei) and with low-density neutron matter. The parameters of the commonly adopted effective forces are usually derived fitting binding energies and other properties of atomic nuclei (mostly magic nuclei) in their ground state, as well as the binding energy of nuclear matter. In some cases also results in neutron matter have been taken into account, but at higher densities than those relevant here. On the other hand, many-body calculations should give reliable results for the equation of state of low-density neutron matter, because the uncertainties related to three-body force play a minor role. The density dependence of neutron matter energy resulting from such calculations has in fact been compared to that of current Skyrme forces (cf. e.g. [2, 21]). We shall make use of the two Skyrme forces SkM* and SLy4, which display a number of attractive properties. The value of the energy per nucleon E/A , calculated with Brückner theory based on a G -matrix derived by the bare nucleon-potential, and shown in Fig. 2, lies in between the results obtained with these two forces. A very relevant quantity in our studies appears to be the effective mass associated with the effective forces. To investigate this point, we have decided to show also results obtained with two other forces: SII and SGII, whose effective mass is close to that of SLy4 and of SkM* respectively (cf. Fig. 1).

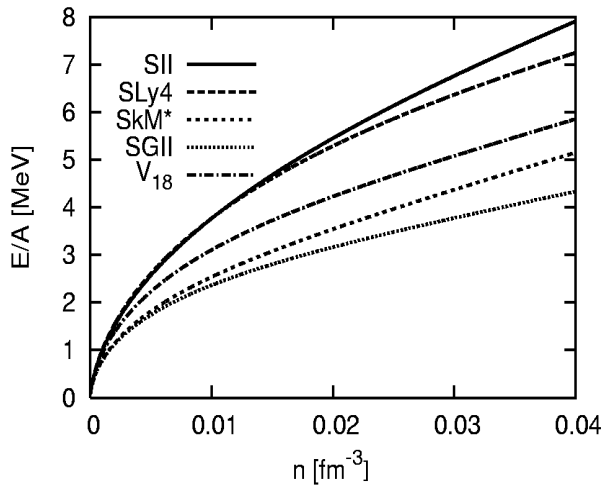


Figure 1: (left) The energy per baryon calculated in neutron matter with Brückner theory with the bare nucleon-nucleon Argonne interaction V_{18} (dot-dashed curve) [21] is compared to the results obtained with the Skyrme interactions SII (solid curve), SLy4 (dashed curve), SkM* (short dashed curve) and SGII (dotted curve).

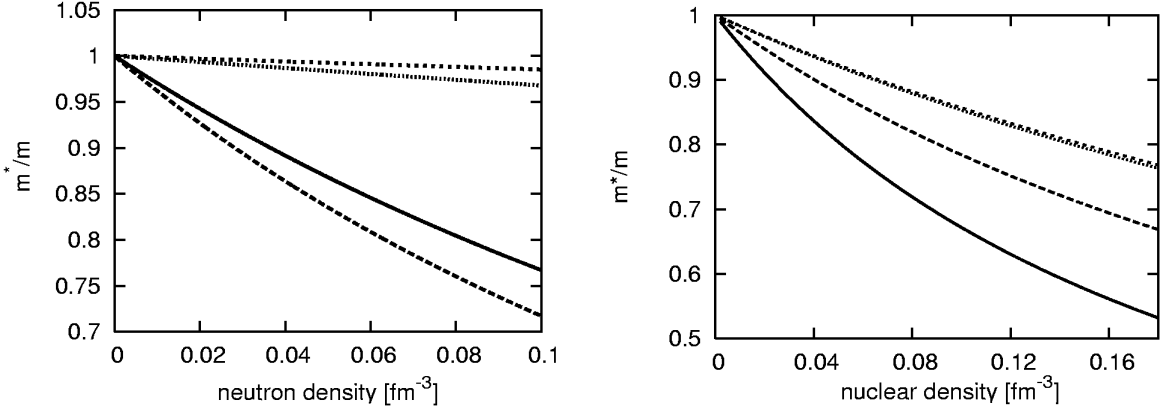


Figure 2: The effective mass in neutron matter (left panel) and in symmetric nuclear matter (right panel) for the different Skyrme interactions used in this paper: SII (solid curve), SLy4 (dashed curve), SkM* (short dashed curve), and SGII (dotted curve).

Concerning the particle-particle channel, we shall use the density dependent contact force

$$V_{pair}(\mathbf{x}, \mathbf{x}') = V_0 \cdot \left(1 - \eta \cdot \left(\frac{n(\mathbf{x})}{0.08} \right)^\alpha \right) \delta(\mathbf{x} - \mathbf{x}'), \quad (3)$$

whose parameters $V_0 = -481$ MeV fm³, $\eta = 0.7$ and $\alpha = 0.45$ have been chosen so as to reproduce the pairing gap of neutron matter obtained making use of a realistic nucleon-nucleon interaction [22]. Because of the zero-range nature of the interaction, all values of the momentum transferred in the nucleon-nucleon interaction processes are allowed. As a consequence one needs to introduce a cutoff parameter E_{cut} . We have implemented this condition in the basis used to calculate the pairing matrix elements (cf. Appendix A), taking only single-particle states with energies lower than $E_{cut} = 60$ MeV. In Fig. 3 we compare the pairing gaps at the Fermi energy calculated in neutron matter with this force and with the bare Argonne nucleon-nucleon potential. In Fig. 3(a) and (b) we use the single-particle levels calculated with the SLy4 and the SkM* interaction respectively: the latter yields higher values of the gap, because of the higher effective mass and thus of the higher single-particle level density. The contact force reproduces rather well the density-dependence of the gap obtained with the bare force, although it underestimates the value at the maximum by 10-20%.

The single-particle potential is obtained self-consistently from the calculated density $n(\mathbf{x}) = \sum_i v_i(\mathbf{x})^2$. We shall follow ref. [23], but we shall neglect the spin-orbit H_{so} and spin coupling H_{sg} terms in the Hamiltonian (cf. the comments at the end of Section IV B

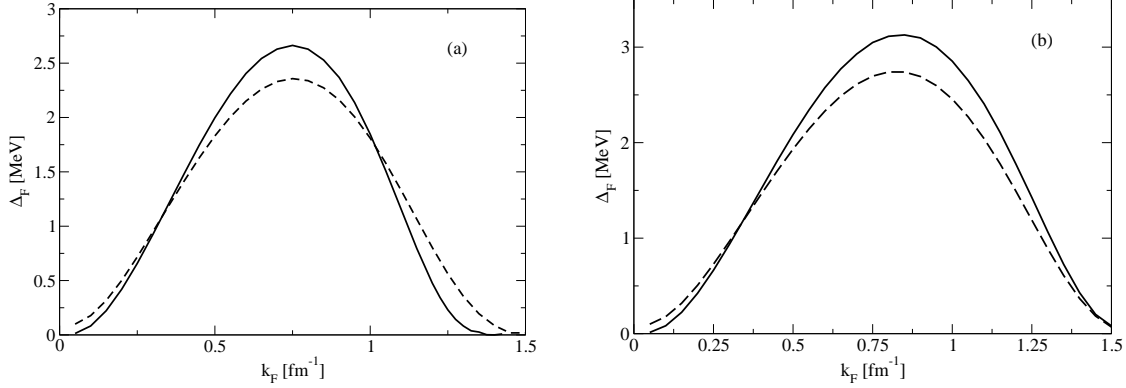


Figure 3: (a) The BCS pairing gap Δ_F in uniform neutron matter at the Fermi energy, is shown as a function of the Fermi momentum $k_F = (3\pi^2 n)^{1/3}$, calculated with the zero-range, density dependent pairing interaction (3) (dashed curve) or with the Argonne interaction (solid curve). In both cases the single-particle levels have been calculated with the SLy4 interaction. (b) The same, but with single-particle levels calculated with the SkM* interaction.

nd Fig. 21). Furthermore, we shall neglect the terms associated with the time-odd momentum density (see for example [26]), which are associated with the presence of the vortex. In fact, we have evaluated their contribution to the energy perturbatively, finding that their contribution is negligible for the scope of this paper.

The pairing gap is obtained self-consistently from the so-called abnormal density $\kappa(\mathbf{x}) = \frac{1}{2} \sum_i u_i(\mathbf{x}) v_i^*(\mathbf{x})$, according to

$$\Delta(\mathbf{x}) = -V_{pair}(\mathbf{x})\kappa(\mathbf{x}). \quad (4)$$

The HFB equations are solved enclosing the system in a cylindrical box of radius $\rho_{box} = 30$ fm and height $h_{box} = 40$ fm (cf. Fig. 4). We assume perfectly reflecting walls, with single-particle wavefunctions which vanish at the edges of the box (see the remarks on this issue in Appendix A).

In the calculations discussed in the following, we shall only consider axial symmetry, in which case the pairing field can be written as [20, 24, 25]

$$\Delta(\rho, z, \phi) = \Delta(\rho, z)e^{i\nu\phi}, \quad (5)$$

ν being the vortex number, which indicates the number of quanta of angular momentum carried by each Cooper pair. In particular, if we set $\nu = 0$ we obtain the usual HFB

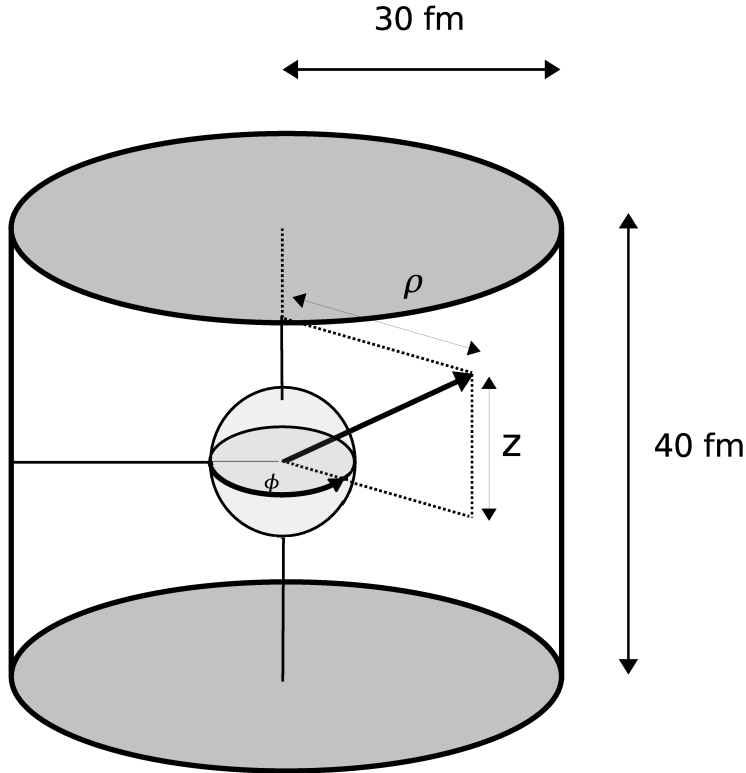


Figure 4: Geometrical features of the cylindrical cell used in most calculations of this paper.

equations (no vortex). Setting instead $\nu = 1$, we can describe a vortex excitation, in which each Cooper pair carries one unit of angular momentum along the z -axis. Experiments on superfluids indicate that it is energetically more favorable to develop an array of $\nu = 1$ vortices rather than a few vortices carrying many quanta of angular momentum and in the following we shall apply this condition also in neutron stars. When $\nu \neq 0$, one obtains a current given by

$$J(r, z, \phi) = -\frac{i\hbar}{m\rho} \sum_i v_i^*(\rho, z, \phi) \frac{\partial v_i(\rho, z, \phi)}{\partial \phi}, \quad (6)$$

and an associated velocity field J/n . Aside from axial symmetry, the system has mirror symmetry respect to the $x - y$ plane (see Fig. 4), so that $\Delta(\rho, z) = \Delta(\rho, -z)$. Applying the parity operator ($\phi \rightarrow \phi + \pi$ and $z \rightarrow -z$) to the pairing field we obtain

$$\hat{P}\Delta(\rho, z)e^{i\nu\phi} = e^{i\nu\pi}\Delta(\rho, z)e^{i\nu\phi}. \quad (7)$$

Therefore the pairing field is an eigenstate of the parity operator with eigenvalue $(-1)^\nu$. This condition implies that the Cooper pairs involved in the $\nu = 1$ excitation are constructed out of single particle levels of opposite parity.

Rather than solving the HFB equations directly in coordinate space, we expand them on a single-particle basis. For details concerning the numerical procedure, we refer to Appendix A.

III. THE PINNING ENERGY

Models that relate the glitch phenomenon to the vortex dynamics in the inner crust, usually assume that the vortex lines which thread the neutron superfluid pin to the crust, being attracted or repelled by the nuclei forming the Coulomb lattice. If the vortex lines remain fixed, the velocity of the superfluid remains constant, while the velocity of the crust decreases due to the magnetic braking. At some critical velocity difference, the Magnus force unpins the vortex lines, and angular momentum is given back to the star, causing the glitch.

The determination of an 'optimal' vortex line depends, besides the lattice properties and the vortex tension, on the vortex-nucleus interaction, or, more precisely, on the free energy as a function of the distance between the nucleus and the vortex axis. As it was mentioned in the Introduction, although in the present paper we shall improve in different ways on previous models, we shall only be able to compare the two limiting configurations: a vortex whose axis passes through the center of the nucleus, and a vortex placed far from the nucleus.

We shall now discuss more precisely how we compute the pinning energy, $E_{pinning}$, at a given density in the crust, following (except for a sign) the definition by Epstein and Baym [10]. At a given density, they calculated, within the Ginzburg-Landau approximation, the energy of the vortex-nucleus system as a function of the distance between the vortex axis and the center of the nucleus, determining the configuration of minimum energy, which often turned out to correspond to zero distance. Then they calculated the pinning energy as the difference between this minimum energy and the energy of a configuration where the vortex and the nucleus are sufficiently far apart, so that their mutual interaction can be neglected. Due to the axial symmetry condition, we shall only compare the energies of the zero-distance configuration (vortex axis passing through the center of the nucleus) and of the non-interacting one. In this framework we only deal with one nucleus at a time, neglecting the interaction of the vortex with distant nuclei. The situation can then be

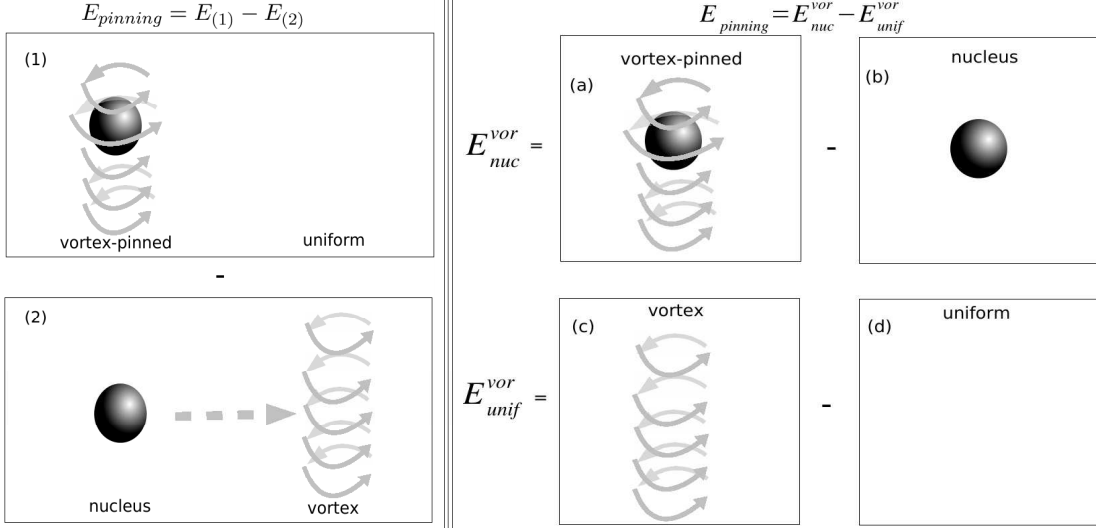


Figure 5: (left) The pinning energy $E_{pinning}$ is obtained taking the difference between the energy of the pinned configuration (1), in which the vortex axis passes through the center of the nucleus, and the energy of the interstitial configuration (2), in which the vortex is far from the nucleus. (right) We rearrange the configurations on the left, indicating that the pinning energy is equivalent to the difference between the energy cost to build the vortex on a nucleus (E_{nuc}^{vor}) and in uniform matter (E_{unif}^{vor}), so that $E_{pinning} = E_{nuc}^{vor} - E_{unif}^{vor}$.

schematically depicted as in the left part of Fig. 5. We have to compare the energies of the *pinned* configuration (1) (vortex axis passing through the center of the nucleus) and of the *interstitial* configuration (2) (vortex axis far from the nucleus). We can then consider $E_{pinning}$ as the difference between two excitation energies:

$$E_{pinning} = E_{nuc}^{vor} - E_{unif}^{vor}, \quad (8)$$

where E_{unif}^{vor} is the energy of a vortex in the uniform matter configuration, compared to the energy of the same configuration in its ground state, while E_{nuc}^{vor} is the energy of the vortex pinned on a nucleus (immersed in the neutron sea), compared to the energy of the isolated nucleus immersed in the neutron sea; that is,

$$\begin{aligned} E_{nuc}^{vor} &= E_{pinned} - E_{nucleus} \\ E_{unif}^{vor} &= E_{vortex} - E_{uniform}, \end{aligned} \quad (9)$$

where the energy associated with each of the four configurations is calculated as described in Appendix A. Pinning the vortex on the nucleus is energetically convenient, if the pinning

energy is negative (note that Epstein and Baym define the pinning energy with the opposite sign). We note that the total and pairing energy of the various configurations, as well as the energy cost to create the vortex, depend on the size of the box. On the contrary, the value of the pinning energy, which is the result of a phenomenon localized on the nucleus, converges for a sufficiently large box.

In practice, four different HFB calculations have to be performed, using the same cylindrical cell (cf. Fig. 6): one with $Z = 40$, $\nu = 1$ (Fig. 6(a)), yielding E_{pinned} ; one with $Z = 40$, $\nu = 0$ (Fig. 6(b)), yielding $E_{nucleus}$; one with $Z = 0$, $\nu = 1$ (Fig. 6(c)), yielding E_{vortex} ; and finally, one with $Z = 0$, $\nu = 0$ (Fig. 6(d)), yielding $E_{uniform}$. To obtain the correct pinning energy it is essential that the calculations refer to the same asymptotic neutron density. In the calculations (b) and (d), without the vortex, we use the same value of the chemical potential λ , yielding $N_{nucleus}$ and $N_{uniform}$ neutrons in the cylindrical cell. The presence of the vortex in calculations (a) and (c) leads in each case to a small decrease of the number of particles. We compensate this reduction by a slight increase in the value of λ . In practice, rather than attempting a very fine tuning of λ we prefer to account for the residual difference in the number of particles subtracting the terms

$$\Delta E_{nuc} = \lambda(N_{pinned} - N_{nucleus}) \quad ; \quad \Delta E_{unif} = \lambda(N_{vortex} - N_{uniform}) \quad (10)$$

respectively to E_{nuc}^{vor} and to E_{unif}^{vor} . Even if the pinning energies represent only a small fraction of the total energy, of the order of $10^{-3} - 10^{-4}$, the subtraction scheme we have just outlined produces numerically reliable results (cf. Appendix B), which will be presented in the next Section. One should notice that the size of the cylindrical cell does not have to coincide with that of the physical Wigner-Seitz cell; it must only be large enough, so as to obtain convergent results for $E_{pinning}$. It is clear, however, that neglecting neighbouring nuclei can be inconsistent, if the radius of the box becomes of the order of the lattice constant. This point will be further discussed below in Section IV C.

IV. RESULTS

We have performed calculations at different densities in the inner crust, ranging between $n \approx 0.001 \text{ fm}^{-3}$ and $n \approx 0.04 \text{ fm}^{-3}$. Our discussion will be mostly based on the results obtained at eight densities with the interaction SLy4 and SkM*, but we shall also present

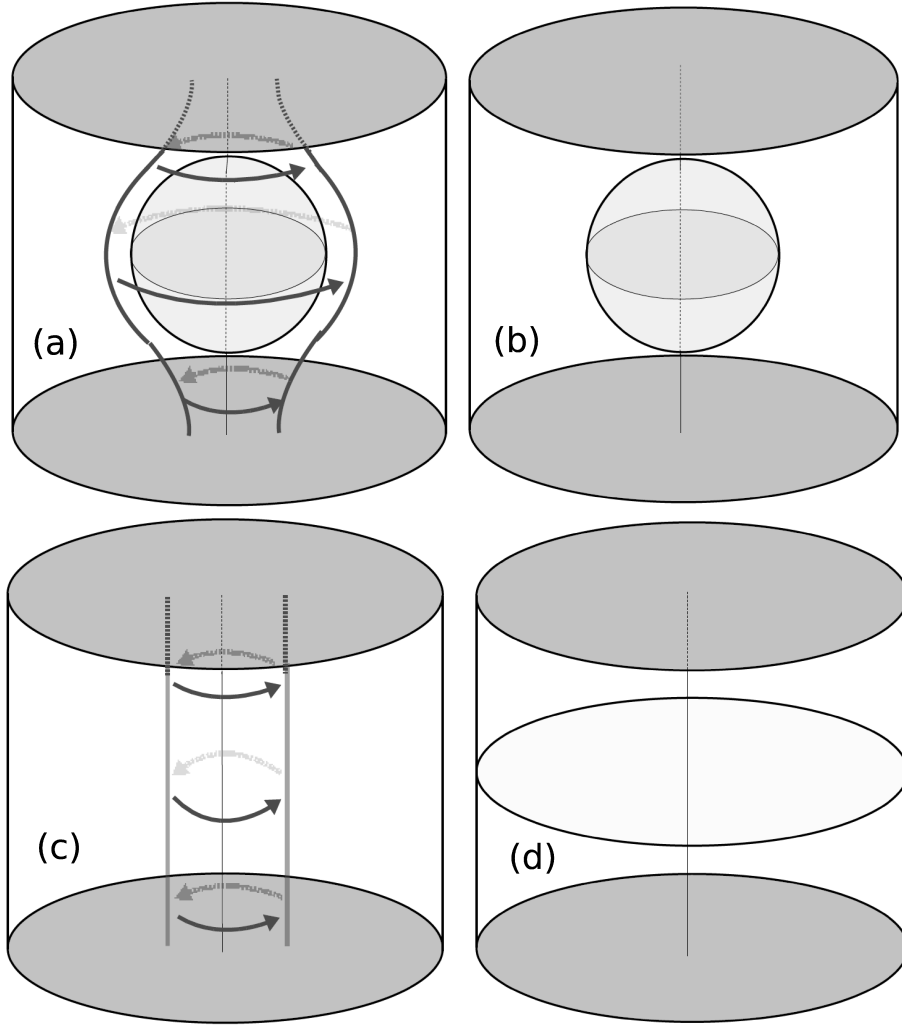


Figure 6: Schematic picture of the four different physical configurations needed to calculate the pinning energy: (a) cell with a vortex pinned on a nucleus ; (b) cell with a nucleus in the neutron sea ; (c) cell with a vortex in the neutron sea; (d) cell in the uniform neutron sea.

results obtained with the interactions SII and SGII (cf. Tables I and II).

In the following we first present the results obtained for a nucleus embedded in the neutron sea, in the absence of vortex (HFB calculations with $\nu = 0$). We then discuss the structure of the vortex ($\nu = 1$), without or with the nucleus. Finally, we present the pinning energies obtained as a function of density.

Interaction	$n_\infty [fm^{-3}]$	$a [fm]$	$n_0 [fm^{-3}]$	$R_0 [fm]$
SLy4	0.001	0.82	0.098	6.06
SLy4	0.002	0.82	0.098	6.04
SLy4	0.004	0.82	0.090	6.81
SLy4	0.008	0.86	0.091	6.75
SLy4	0.011	0.91	0.089	6.76
SLy4	0.017	0.96	0.081	7.33
SLy4	0.026	1.05	0.070	7.83
SLy4	0.037	1.13	0.057	8.43
SII	0.001	0.73	0.093	6.15
SII	0.002	0.73	0.093	6.14
SII	0.004	0.74	0.092	6.10
SII	0.008	0.77	0.086	6.74
SII	0.011	0.78	0.085	6.71
SII	0.016	0.81	0.082	6.75
SII	0.024	0.87	0.073	7.18
SII	0.035	0.94	0.062	7.60

Table I: Parameters of the Fermi function (11), fitting the calculated neutron densities in the Wigner Seitz cells with the SLy4 and SII interactions. The values of the density have been rounded off at the third digit.

Interaction	n_∞ [fm^{-3}]	a [fm]	n_0 [fm^{-3}]	R_0 [fm]
SkM*	0.001	0.88	0.097	6.12
SkM*	0.002	0.90	0.097	6.17
SkM*	0.004	0.96	0.091	6.76
SkM*	0.008	0.97	0.088	6.73
SkM*	0.012	1.00	0.086	6.78
SkM*	0.016	1.05	0.080	7.03
SkM*	0.025	1.09	0.070	7.33
SkM*	0.038	1.17	0.054	7.95
SGII	0.001	0.86	0.097	6.91
SGII	0.002	0.88	0.097	6.91
SGII	0.004	0.90	0.096	6.82
SGII	0.008	0.94	0.092	6.86
SGII	0.011	1.00	0.086	7.34
SGII	0.016	1.00	0.082	7.38
SGII	0.026	1.07	0.070	7.77
SGII	0.037	1.13	0.057	8.27

Table II: Parameters of the Fermi function (11), fitting the calculated neutron densities in the Wigner Seitz cells with the SkM* and SGII interactions. The values of the density have been rounded off at the third digit.

A. Calculations with $\nu = 0$

We first discuss the density and the pairing gaps obtained solving the HFB equations for $\nu = 0$ in the cylindrical box, for the nuclei immersed in the neutron sea at the various densities. The pairing field in the Wigner-Seitz cell has been studied by various groups, either based on Woods-Saxon potentials [27] or on selfconsistent HFB calculations with Skyrme forces [18, 28, 29]. The effects of temperature, and the specific heat, have also been discussed [27, 29], but we shall limit ourselves to zero temperature. Our calculations are performed assuming axial symmetry, and they should respect the spherical symmetry of isolated nuclei. In our calculations the neutron density is a function of the coordinates ρ and z . To test the sphericity of our calculations we evaluate the mean value of the density within a spherical shell 0.05 fm wide and centered around a mean distance r from the center of the nucleus and then evaluate the fluctuations at every point. The relative error (rms/average density) is everywhere lower than 0.03.

As first remarked by Negele and Vautherin [1], nuclei in the inner crust turn out to be fatter than atomic nuclei, due to their interaction with the neutron sea. We have fitted the neutron density resulting from our calculations with a Fermi function:

$$f(r) = n_\infty + \frac{n_0}{\left(1 + \exp\left(\frac{(r-R_0)}{a}\right)\right)}, \quad (11)$$

where n_∞ gives the asymptotic value of the neutron density far from the nucleus, and we have determined the values of n_0 , R_0 and a which best reproduce the computed density profile and are reported in Tables I and II. In the calculations we have adjusted the value of λ so as to obtain the same set of values of n_∞ for the various interactions, but there remain slight differences in a few values (cf. also Tables III and IV). We compare the calculated and fitted densities for three cases in Fig. 7. The diffusivity a increases from about 0.7 to about 1.1 fm with increasing density, to be compared with the typical value of 0.65 fm for finite nuclei, and the radius R_0 (up to 8 fm at the highest densities) also turns out to be rather large compared to ordinary nuclei.

In Figs. 8-10 we show the pairing gaps and selfconsistent potentials as a function of the distance from the nucleus, calculated for $n_\infty \approx 0.001, 0.01$ and 0.035 fm^{-3} ; the associated effective masses are shown in Fig. 11.

As we anticipated (cf. Fig 2), the behaviour of the forces can be divided into two groups:

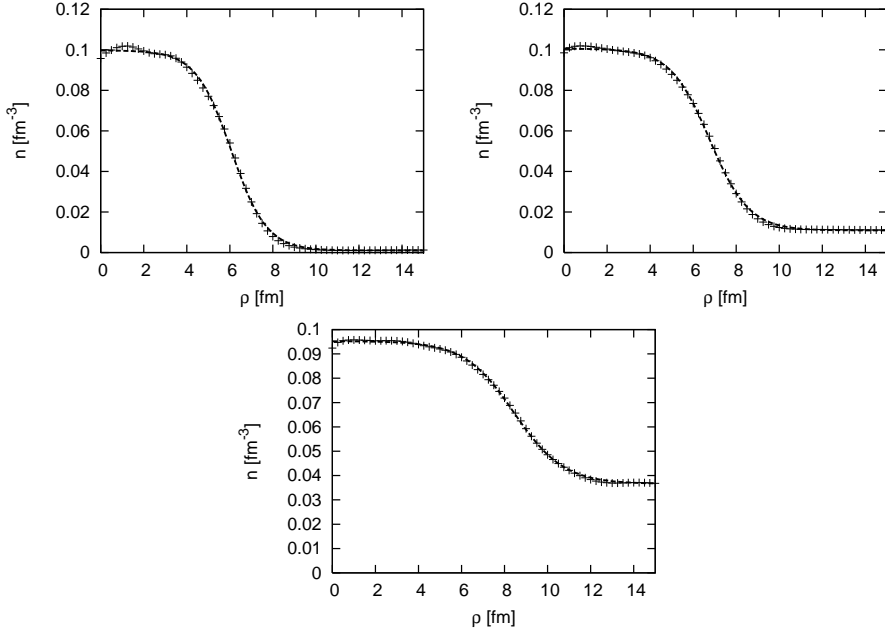


Figure 7: The neutron density calculated in the cylindrical box with the nucleus on the $z = 0$ plane (crosses) is compared with the fit obtained with the Fermi function (cf. Eq. 11). As we discuss in the text, the calculated density is spherically symmetric to a good approximation. The figures refer to the asymptotic densities $n_\infty = 0.001, 0.011$ and 0.037 fm^{-3} , and have been computed with the SLy4 interaction.

the effective masses associated with SGII and SkM* are quite similar ($m^*/m \approx 0.9$ in the interior of the nucleus), as are those associated with SLy4 and SII ($m^*/m \approx 0.7$). In order to reproduce the same asymptotic density the SII and SLy4 interactions produce a deeper selfconsistent potential than the SkM* and SGII. In all cases the pairing gap increases, going from the nuclear region to the sea of superfluid neutrons. This is in keeping with the density dependence of the pairing gap in uniform matter, previously shown in Fig. 3: the interior of the nucleus corresponds to large values of the local Fermi momentum where the pairing gap tends to vanish, while even at the smallest densities considered here, the gap in neutron matter is at least close to 1 MeV. In the case of the SkM* and SGII interactions the pairing gaps show a peak in the nuclear surface region for $n_\infty \approx 0.001 \text{ fm}^{-3}$ (cf. Fig. 8). The pairing gaps are smaller with SII and SLy4, due to their lower effective mass and level density.

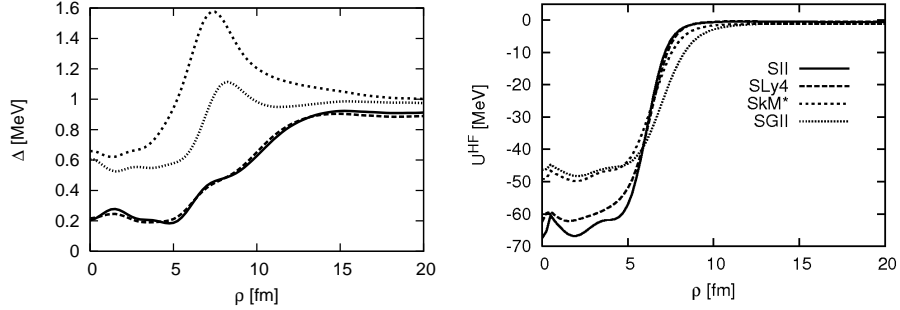


Figure 8: Pairing gap (left) and selfconsistent potential (right) in the cylindrical cell without the vortex ($Z = 40, \nu = 0$) for $n_\infty \approx 0.001 \text{ fm}^{-3}$ ($k_F \approx 0.3 \text{ fm}^{-1}$). The different interactions are: SLy4 (dashed curve), SkM* (short dashed curve), SII (solid curve), and SGII (dotted curve).

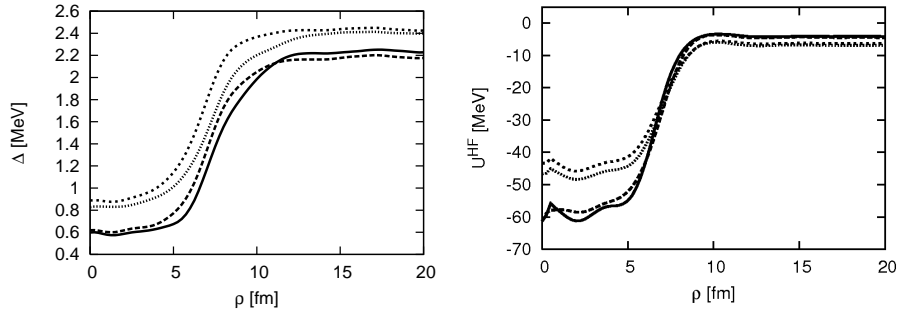


Figure 9: Pairing gap (left) and selfconsistent potential (right) in the cylindrical cell ($Z = 40, \nu = 0$) for $n_\infty \approx 0.011 \text{ fm}^{-3}$ ($k_F \approx 0.7 \text{ fm}^{-1}$). The different interactions are: SLy4 (dashed curve), SkM* (short dashed curve), SII (solid curve) and SGII (dotted curve).

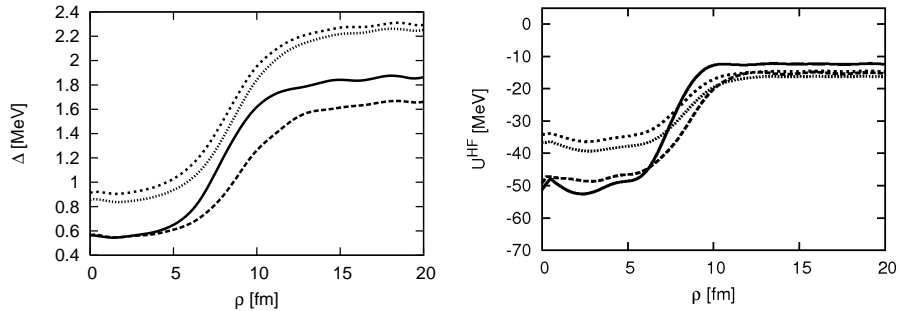


Figure 10: Pairing gap (left) and selfconsistent potential (right) in the cylindrical cell ($Z = 40, \nu = 0$) for $n_\infty \approx 0.035 \text{ fm}^{-3}$ ($k_F \approx 1 \text{ fm}^{-1}$). The different interactions are: SLy4 (dashed curve), SkM* (short dashed curve), SII (solid curve), and SGII (dotted curve).

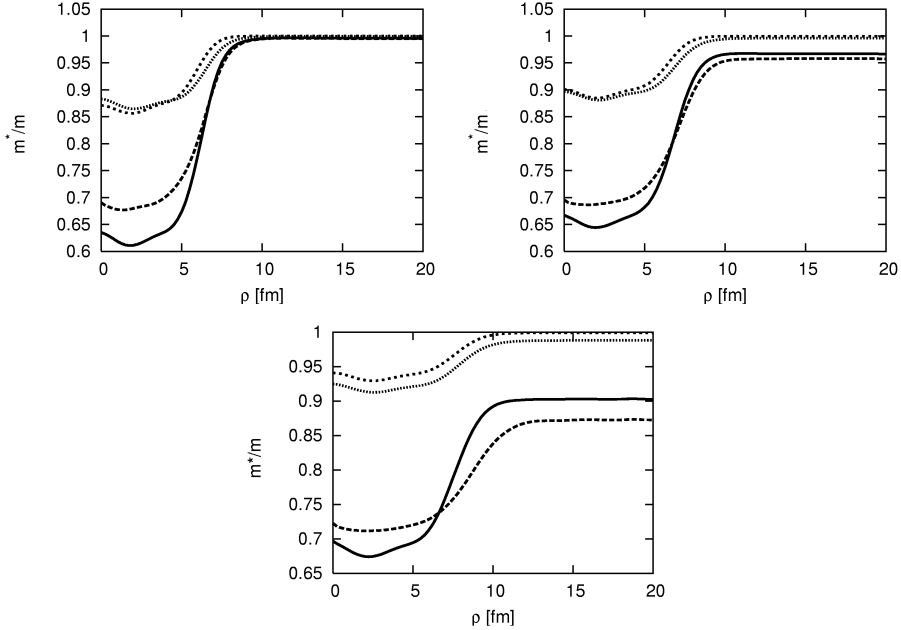


Figure 11: Effective masses associated with the calculations presented in Fig. 8 ($n_\infty \approx 0.001 \text{ fm}^{-3}$, top left), in Fig. 9 ($n_\infty \approx 0.01 \text{ fm}^{-3}$, top right), and in Fig. 10 ($n_\infty \approx 0.035 \text{ fm}^{-3}$, bottom) for the four interactions SII (solid curve), SLy4 (dashed curve), SkM* (short dashed curve) and SGII (dotted curve).

B. Calculations with $\nu = 1$

We now turn our attention to the HFB calculations of the vortex ($\nu = 1$). We first discuss the results we obtain for the uniform neutron sea ($Z = 0$). In this case the vortex configuration keeps cylindrical symmetry, and a cut at a fixed value of z provides complete information. The density profiles and the pairing gap obtained with the SLy4 interaction at four different densities are reported in Fig. 12. The pairing gap vanishes on the vortex axis, and grows linearly for about 3-5 fm; then it slowly increases towards the value in $\nu = 0$ neutron matter. In keeping with Fig. 3, the asymptotic value of Δ reaches its maximum for $k_F \sim 0.8 \text{ fm}^{-1}$, that is, for $n \sim 0.02 \text{ fm}^{-3}$. Near the vortex axis the pairing gap displays oscillations that have been interpreted as Friedel-like oscillations, due to the presence of bound states in the vortex core [30]. Our results are very similar to those obtained by Bulgac and Yu, who have solved the HFB equations for a vortex in uniform, infinite neutron matter for the first time [13]. In particular, the depletion of the density close to the vortex axis (cf. Fig. 12) and the behaviour of the velocity field (cf. Fig. 13) are in good agreement

with their results. Note however that we use a different pairing interaction and that we consider densities larger than those calculated in ref. [13].

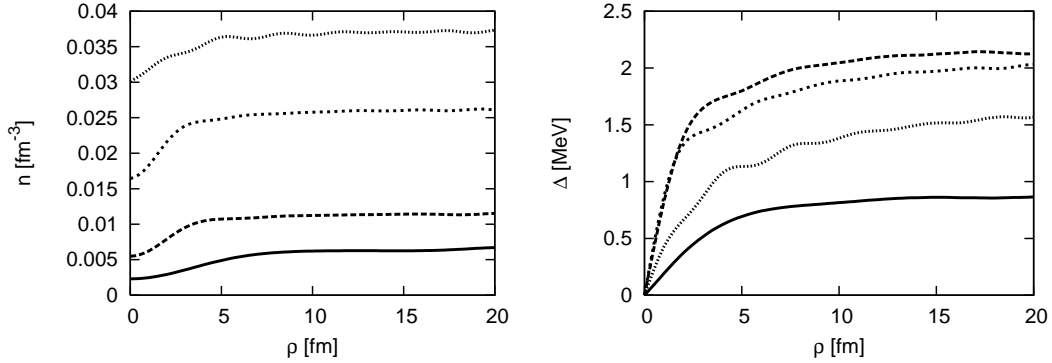


Figure 12: (left) Neutron density profiles for the vortex solution, without the nucleus at the center of the cell ($Z = 0, \nu = 1$), calculated with the SLy4 interaction at different densities: $n_\infty = 0.0013 \text{ fm}^{-3}$; (solid curve, the density shown has been multiplied by 5), $n_\infty = 0.011 \text{ fm}^{-3}$; (dashed curve), $n_\infty = 0.026 \text{ fm}^{-3}$ (short dashed curve) and $n_\infty = 0.037 \text{ fm}^{-3}$; (dotted curve). (Right) The corresponding pairing gaps.

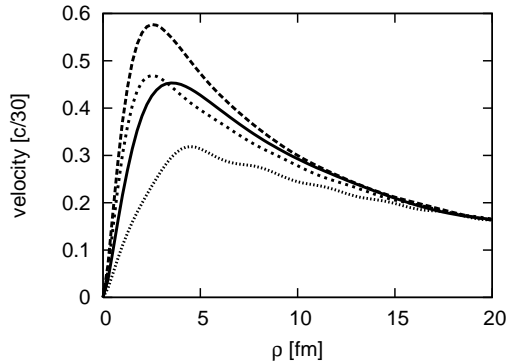


Figure 13: Velocity field of a vortex calculated in the cell without the nucleus ($Z = 0, \nu = 1$), with the SLy4 interaction calculated with $n_\infty = 0.0013 \text{ fm}^{-3}$; (solid curve), $n_\infty = 0.011 \text{ fm}^{-3}$; (dashed curve), 0.026 fm^{-3} ; (short dashed curve), and 0.037 fm^{-3} ; (dotted curve). For large values of ρ the velocity tends to the Onsager limit $\hbar/2m\rho$.

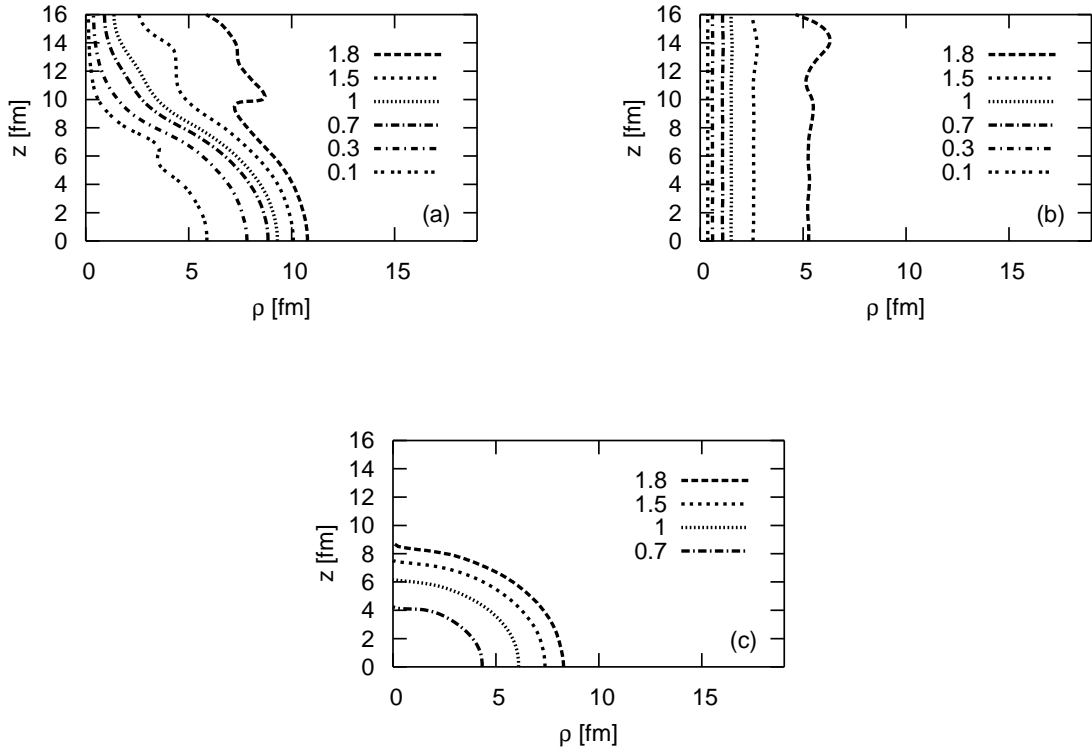


Figure 14: The level curves (values in MeV) of the pairing gap associated with a vortex pinned on a nucleus ($Z = 40, \nu = 1$, top left), with a vortex in uniform matter ($Z = 0, \nu = 1$, top right) and with a nucleus in the neutron sea ($Z = 40, \nu = 0$, bottom) obtained with a SLy4 force for $n_\infty = 0.011 \text{ fm}^{-3}$. The nucleus is at $\rho = z = 0$ and the vortex is along the z -axis.

We now discuss the calculation of the vortex pinned on the nucleus ($Z = 40, \nu = 1$). The main results are illustrated in Figs. 14 and 15, which refer to a calculation performed at $n_\infty = 0.011 \text{ fm}^{-3}$ with the SLy4 interaction. In Fig. 14 we show the gap in the ρ, z plane. In Fig. 15 the gap is shown as a function of ρ in the $z = 0$ equatorial plane. In Fig. 15 we also make a comparison with the pairing gaps obtained for a vortex in uniform matter and for a nucleus in the neutron sea, previously discussed. The neutron density and the velocity field are shown in Fig. 16.

For large values of z the properties of the vortex are the same as those calculated for uniform matter (cf. Fig. 14). Approaching the nuclear surface the vortex is strongly modified, and the associated pairing gap is suppressed within its volume and also on its surface (for example $\Delta \approx 0.3 \text{ MeV}$ at $\rho \approx 7 \text{ fm}$ and $z = 0$), both compared to the case of an isolated

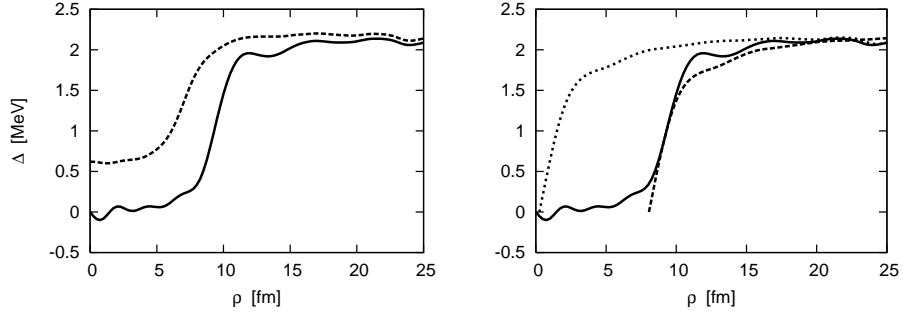


Figure 15: (left) The pairing gap associated with the pinned vortex on the $z = 0$ plane ($Z = 40, \nu = 1$, solid line) is compared with the gap associated with the nucleus in the absence of the vortex ($Z = 40, \nu = 0$, dashed line). (right) The pairing gap associated with the pinned vortex ($Z = 40, \nu = 1$, solid line) is now compared to the gap associated with the vortex in uniform matter ($Z = 0, \nu = 1$, short dashed line); the latter is also shown translated by 7.8 fm (dashed line). The calculation is for the SLy4 interaction at $n_\infty = 0.011 \text{ fm}^{-3}$.

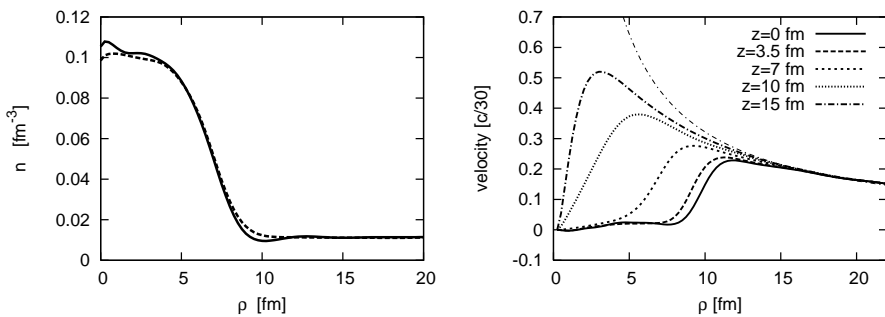


Figure 16: (left) Density with ($Z = 40, \nu = 1$, solid line) and without ($Z = 40, \nu = 0$, dashed line) the vortex, calculated at $n_\infty = 0.011 \text{ fm}^{-3}$ on the $z = 0$ plane with the SLy4 force. (right) Velocity field of the pinned vortex. The different curves refer to different cuts; the dot-dashed line is the $\hbar/2m\rho$ function.

nucleus in the absence of the vortex ($\Delta \approx 1$ MeV) and compared to the case of a vortex in uniform neutron matter ($\Delta \approx 2$ MeV). The typical linear rise of the gap away from the vortex axis is delayed by about 8 fm, which is about the radius of the nucleus, as compared to the uniform case (cf. Fig. 15). In other words, the vortex opens up and surrounds the nuclear volume, being unable to penetrate into it. The suppression of the $\nu = 1$ pairing field inside the nucleus was already found (but not thoroughly discussed) in a quantum calculation by Elgarøy and De Blasio [30], although their study was not self-consistent and assumed an unrealistic cylindrical shape for the nucleus. The same effect appears concerning the velocity of the vortex flow. The velocity vanishes inside the nuclear volume, and the typical rise of the velocity field from zero to the asymptotic Onsager dependence $v = \hbar/2m\rho$ is delayed, again by about 8 fm at $z = 0$. The vortex induces some changes on the nuclear density, which becomes somewhat elongated along the vortex axis, increases close to the center of the nucleus and decreases close to the surface, mostly around the equatorial plane (cf. Fig. 16). This behaviour can be compared with the case of the vortex in uniform matter, where the depletion takes place close to the axis (cf. Fig. 12 above).

The pairing gaps calculated for the four configurations at $n_\infty \sim 0.001, 0.01$ and 0.035 fm $^{-3}$ with the interactions SLy4 and SkM* are collected in Figs. 17-19. The results obtained with SLy4 at all densities reflect the main features discussed above (the results obtained with the SII interaction are very similar). One can observe that at the highest density, the results obtained with the SkM* interaction show a different behaviour. In fact, in this case the pairing gap associated with the vortex is not suppressed in the interior of the nucleus, but it shows a constant increase: the vortex can penetrate the nucleus. Differences are present also in the density (which presents a slight depletion close to the vortex axis) and in the velocity (which does not go to zero in the interior of the nucleus), which are closer to the case of the vortex in uniform matter. The pairing gap associated with the pinned vortex obtained with the SkM* (and with the SGII) interaction can be approximated rather well assuming that the gap suppressions produced by the nuclear field ($\Delta_{nucleus}(\rho)/\Delta_\infty$) and by the vortex in uniform matter ($\Delta_{vortex}(\rho)/\Delta_\infty$) respect to the value in uniform matter Δ_∞ act simultaneously and independently (cf. Fig. 20). The superposition of the effects is then the product of the two suppressions:

$$\Delta(\rho) = (\Delta_{vortex}(\rho)/\Delta_\infty) \cdot (\Delta_{nucl}(\rho)/\Delta_\infty) \cdot \Delta_\infty. \quad (12)$$

This approximation would fail badly in the case of SLy4 interaction, where the pairing of the pinned vortex is suppressed much more strongly in the interior, as discussed above.

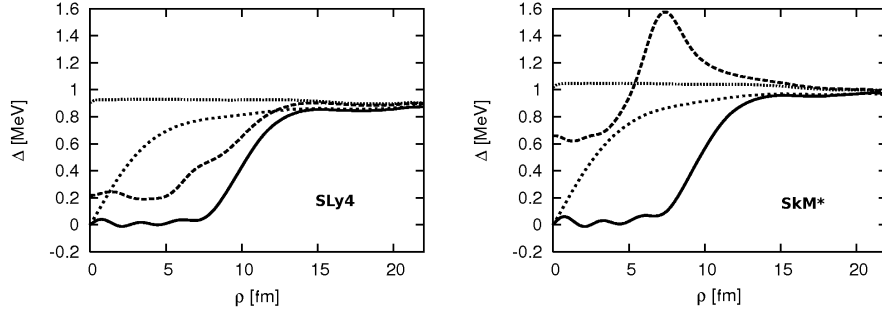


Figure 17: The pairing gaps associated with the four different configurations (pinned vortex ($Z = 40, \nu = 1$): solid curve; nucleus in the neutron sea ($Z = 40, \nu = 0$): dashed curve; vortex the neutron sea ($Z = 0, \nu = 1$): short dashed curve; uniform neutron sea ($Z = 0, \nu = 0$: dotted curve)) calculated with the SLy4 (left) and the SkM* (right) interactions at $n_\infty \sim 0.001 \text{ fm}^{-3}$.

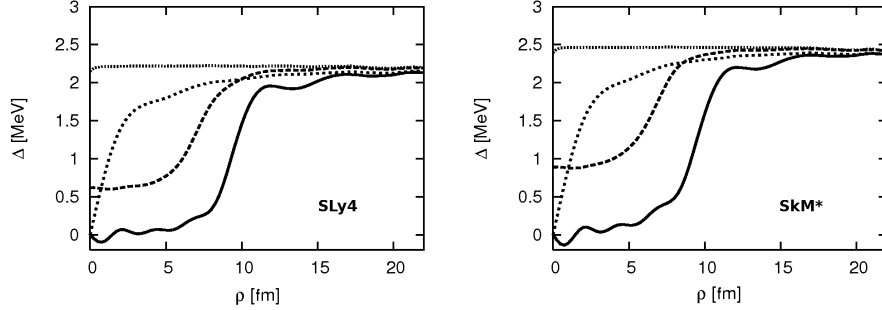


Figure 18: The same as Fig. 17, but for the density $n_\infty \sim 0.01 \text{ fm}^{-3}$.

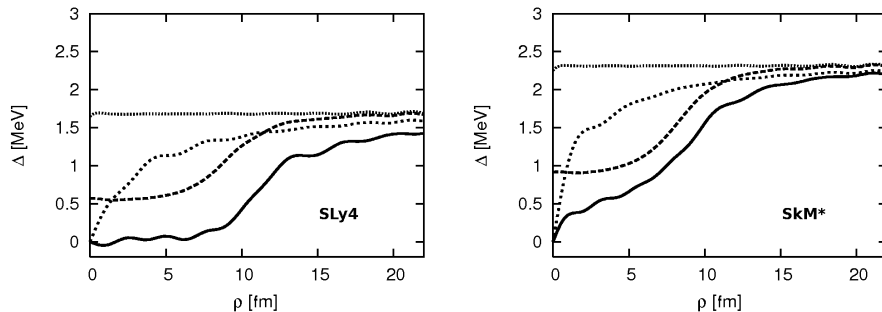


Figure 19: The same as Fig. 17, but for the density $n_\infty = 0.035 \text{ fm}^{-3}$.

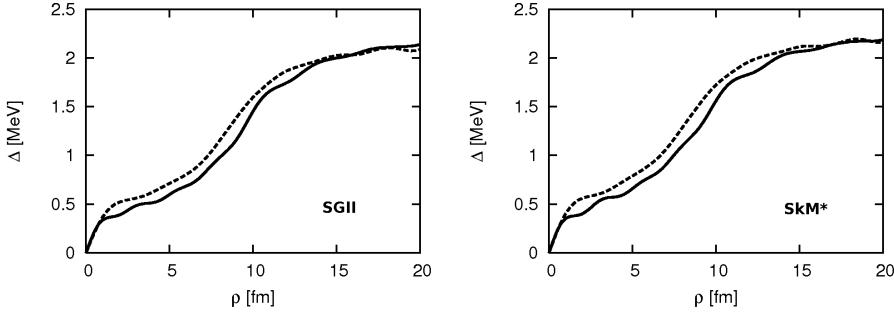


Figure 20: The pairing gaps calculated with the SGII (left) and the SkM* (right) interactions at $n_\infty \sim 0.035 \text{ fm}^{-3}$ (solid lines) are compared with the expression (12) (dashed lines).

The different behaviours discussed above can be understood qualitatively in terms of nuclear shell effects. As we remarked previously, the $\nu = 1$ Cooper pairs are formed out of single-particle levels of opposite parity. Shell effects strongly hinder the formation of such Cooper pairs inside the nuclear volume, as they separate the levels of opposite parity lying within the nuclear potential (i.e. the resonant states) by several MeV, even if these levels lie in the continuum. This can be seen in Fig. 22(a) and (b), where we show a calculation of the phase shifts $\delta_l(E)$, for $l = 0 - 10$, in the mean field (without the vortex) associated with the interaction SLy4 at the densities $n_\infty = 0.011 \text{ fm}^{-3}$ (cf. Fig. 9) and $n_\infty = 0.037 \text{ fm}^{-3}$ (cf. Fig. 10). In the figures the energy E is referred to the asymptotic value V_∞ of the self-consistent potential U^{HF} far from the nucleus (cf. Fig. 9 and Fig. 10). In Fig. 22(c) and (d) we show the same calculation for the SkM* interaction. We recall that the resonant states and the resonant energy are characterized by the conditions $\delta_l(E_{res}) = (2n + 1)\pi/2$, $n = 0, 1, \dots$, and $d\delta_l(E_{res})/dE > 0$, which in the present cases are fulfilled by states with energies up to about 30-40 MeV. At low density (cf. Fig. 22(a) and (c)) the phase shifts are similar for the two interactions. Close to the Fermi energy $\lambda - V_\infty$, which is about 10 MeV, one finds a rather narrow resonance for $l = 7$ ($\Gamma = \pi/(d\delta_l(E_{res})/dE) \approx 3 \text{ MeV}$); one also finds narrow resonances for $l = 6$ ($\Gamma \approx 0.5 \text{ MeV}$) and rather well defined resonances for $l = 8$ ($\Gamma \approx 15 \text{ MeV}$), but they lie about 7 MeV below or above the Fermi energy.

In Fig. 22(b) and (d) we show a calculation at higher density, corresponding to $\lambda - V_\infty$ about 25 MeV. One still finds resonant states in the region around the Fermi energy, associated with $l = 8 - 9$, but they are much broader for the SkM* (the width becoming larger than the centroid energy) than for the SLy4 interaction ($\Gamma \approx 9 \text{ MeV}$ compared to

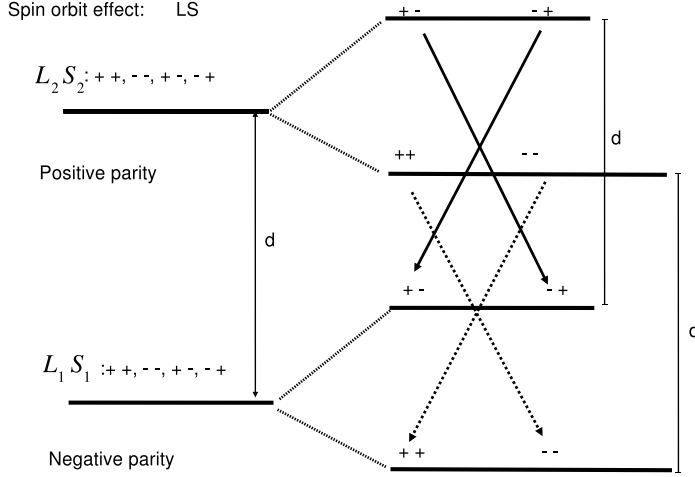


Figure 21: Schematic figure showing that the spin-orbit interaction tends to shift the energy of single-particle pairs involved in the formation of $S = 0, \nu = 1$ Cooper pairs by the same amount (cf. text).

$E_{res} - V_\infty \approx 15$ MeV for $l = 8$, and Γ is still of the order of $E_{res} - V_\infty$ for $l = 9$), in keeping with the fact that the mean-field potential is much shallower. The role of shell effects in the SkM* case is correspondingly much reduced, and the pairing interaction is able to mix levels of opposite parity and to create a pairing field of $\nu = 1$ character inside the nuclear volume.

This interpretation is reinforced by a calculation of a $\nu = 2$ vortex. In this case, Cooper pairs are formed out of single-particle states of the same parity, and one can see in Fig. 23 that already for $n_\infty = 0.011$ fm $^{-3}$ the pairing gap obtained with the SLy4 interaction does not vanish within the nucleus: its value can be reproduced by the simple approximation of Eq. (12), similar to the case of the SkM* interaction at high density (cf. Fig. 20).

It could be argued that the spin-orbit interaction, not considered in the present calculation, will shift the relative energies of levels of different parity around the Fermi energy, eventually modifying the pairing gap we obtain. However the $\nu = 1$ pairing field connects single-particle levels with opposite spin projections, and with L_z -values such that $L_z(1) + L_z(2) = \nu$. This implies (except for $L_z = 0 - 1$) that the products $L_z(1) * S_z(1)$ and $L_z(2) * S_z(2)$ have the same sign, so that the two levels will be shifted by about the same amount by the spin-orbit interaction, as illustrated in Fig. 21. One thus does not expect a

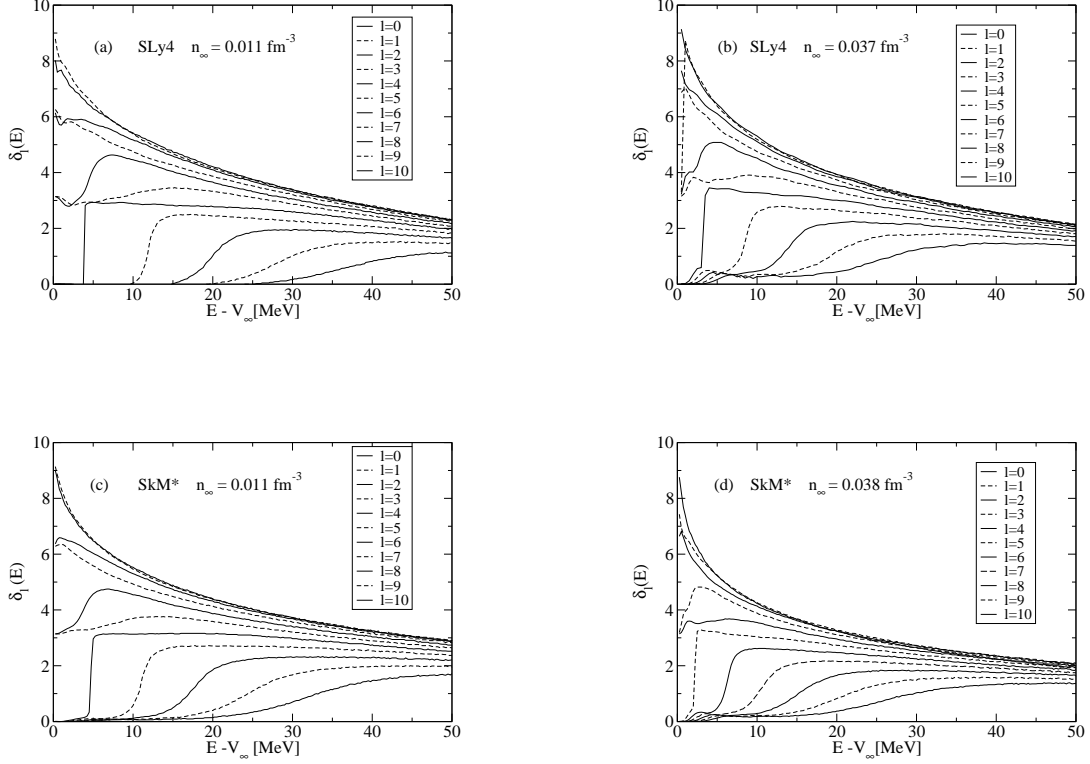


Figure 22: Phase shifts associated with the Hartree-Fock potential for a spherical nucleus, obtained with the SLy4 interaction for $n_\infty = 0.011 \text{ fm}^{-3}$ (corresponding to $\lambda = 5.8 \text{ MeV}$ (a)) and for $n_\infty = 0.037 \text{ fm}^{-3}$ (corresponding to $\lambda = 11.3 \text{ MeV}$ (b)), and with the SkM* interaction for $n_\infty = 0.011 \text{ fm}^{-3}$ (corresponding to $\lambda = 5.8 \text{ MeV}$ (c)), and for $n_\infty = 0.038 \text{ fm}^{-3}$ (corresponding to $\lambda = 11.3 \text{ MeV}$ (d)). The energy is referred to the asymptotic value of the mean field potential far from the nucleus.

significant change of the phase space density relevant for the vortex formation.

C. Pinning energies

We now turn to the calculation of the pinning energy, defined above in Section III. We recall that we compare the energy of the 'pinned' configuration (vortex axis passing through the center of the nucleus) with the 'interstitial' configuration, in which we assume that the vortex is placed far from the nuclei, so that its properties are the same as in uniform matter. In both cases, we assume that the interaction of the vortex with 'distant' nuclei can be neglected. In order to address the validity of our approximation in a quantitative way, one would need to perform systematic calculations taking into account the band structure

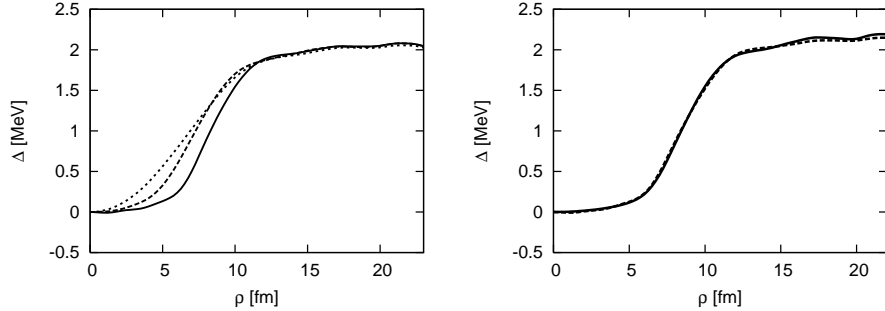


Figure 23: (left): The pairing gap associated with a $\nu = 2$ vortex pinned on the nucleus ($Z = 40, \nu = 1$), calculated with the SLy4 interaction at $n_\infty = 0.011 \text{ fm}^{-3}$. The cuts refer to fixed value of $z = 10 \text{ fm}$ (short dashed curve), $z = 5 \text{ fm}$ (dashed line) and $z = 0 \text{ fm}$ (solid line). (right) The pairing gap at $z = 0$ (dashed line) is compared to the approximation (12) (solid line) .

associated with the lattice [5]. One expects, however, that our approximation should be reasonable if the vortex radial dimension is smaller than the distance between nuclei, as given by the diameter of the Wigner-Seitz cell calculated by Negele and Vautherin. To obtain some insight about this point, we need an estimate of the extension of the vortex. Different definitions of the vortex radius in uniform matter have been introduced. One often

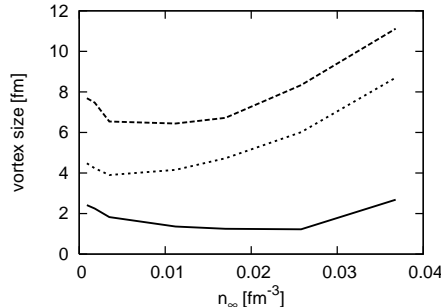


Figure 24: Comparison between different definitions of the vortex radius: $R_{50\%}$ (solid curve), $R_{90\%}$ (dashed curve) and coherence length (short dashed curve), calculated with the SLy4 interaction for a vortex in uniform neutron matter at various neutron densities.

employs the coherence length, $\xi = \hbar^2 k_F / m \pi \Delta$, shown in Fig. 24 by the short-dashed curve. We also show two different estimates of the vortex radius [30], namely the distances $R_{90\%}$ or $R_{50\%}$ from the axis where the pairing gap reaches 90% or 50% of its asymptotic value. According to this figure, the coherence length and $R_{90\%}$ display a similar dependence on

density, while the quantity $R_{50\%}$ is small and almost independent of the density. We shall take $R_{90\%}$ as a measure of the vortex radius, as this is the most conservative estimate.

Let us then consider the interstitial configuration first.

In this case we require that when the vortex has reached its asymptotic gap, the neutron density is still close to its asymptotic n_{infty} , that is, it is not appreciably affected by the neighbouring nuclei. We then introduce the distance $R_{safe} \equiv R_{WS} - 1.2R_N$. According to the parametrization (11), the quantity R_{safe} represents the distance where the difference between the neutron density and its asymptotic value has reduced to 10% of its maximum value. It turns out (see Fig. 26) that the dimension of the vortex is always smaller than R_{safe} , although it approaches this value at the largest densities we have considered in our calculations.

Concerning the pinned configuration, the radii of the pinned vortices, measured through $R_{90\%}$, are 4-6 fm larger than in uniform matter, depending on the interaction (cf. Fig. 25). However, the neglect of neighbouring nuclei appears to be even better justified for the pinned than for the interstitial configuration discussed previously. In fact, in the pinned case one should compare $R_{90\%}$ with the distance between neighbouring nuclei $2R_{WS}$ (or better with $2R_{safe}$). In all cases the calculated radii of the pinned vortices are considerably smaller than this value.

Consequently we can safely describe the structure of the vortex in the inner crust, both in the interstitial and in the pinned configuration, within cylindrical boxes of the order of $R_{90\%}$. However, in the calculation of the pinning energy we need a common box size value for the two vortex configurations. This implies using a box of radius close to the value $R_{90\%}$ for the pinned configuration, which is the largest one: this quantity remains smaller than R_{safe} , as can be seen comparing Fig. 25 with Fig. 26.

In practice we have used somewhat larger radii in the calculation of the pinning energy in order to check that our boundary conditions do not produce any relevant effect (see appendix A).

The fact that the presence of neighbouring nuclei is not relevant for the calculation of the pinning energy for the densities considered in this paper, is confirmed by explicit estimates carried out in refs. [10, 11] (see Appendix C).

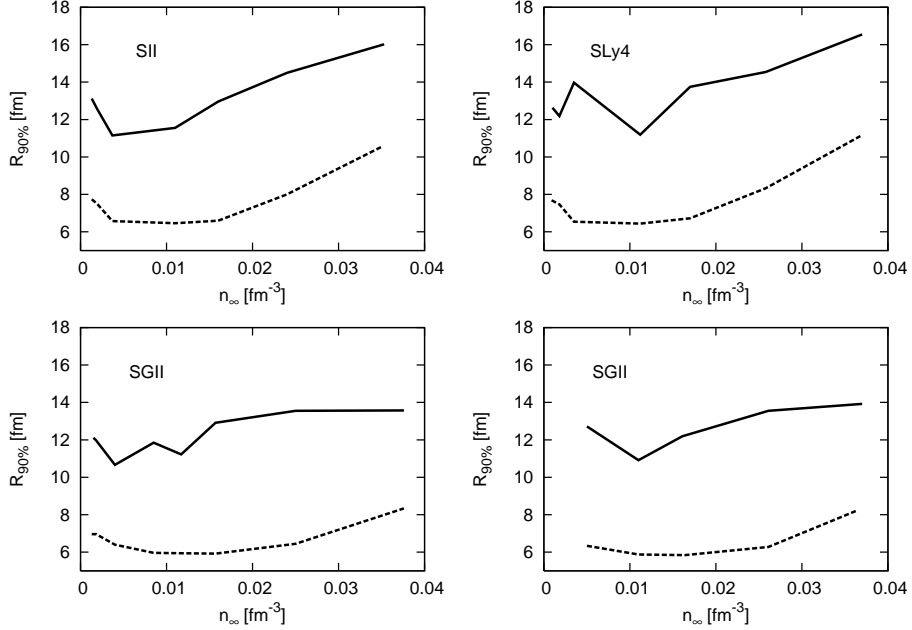


Figure 25: The vortex radius, $R_{90\%}$ is shown for the pinned vortex (solid curves) and for the vortex in uniform matter (dashed curves), for the four Skyrme interactions.

After calculating the energies of the four different configurations of Fig. 6, and using Eqs.(8) and (9) we compute the pinning energies shown in Fig. 27 for different values of λ and n_∞ (cf. Tables I and II). An estimate of the numerical errors associated with the calculations is given in Appendix B. Some details of the energy calculations performed with the interactions SLy4 and SkM* are reported in Tables III and IV, in which we list the values of the chemical potential, of the number of neutrons, of the total energy E_{tot} and of the pairing energy E_{pair} (cf. Appendix A). The total energy associated with the two calculations with a vortex (labeled 'Pinned' and 'Vortex'), has been corrected by the term ΔE introduced at the end of Section III, in order to account for the difference in number of neutrons compared to the corresponding calculations without vortex (labeled 'Nucleus' and 'Uniform').

All the interactions yield weak pinning ($E_{pinning} \lesssim 0$) at the smallest densities we have calculated ($n_\infty \sim 0.001$ fm $^{-3}$), and yield a few MeV antipinning for $n_\infty = 0.01 - 0.02$ fm $^{-3}$. At higher density, the SkM* and SGII interaction lead to a strong antipinning ($E_{pinning} > 0$), in marked contrast with the other two interactions, which instead again produce weak pinning at the highest density points. This different density dependence can be related to

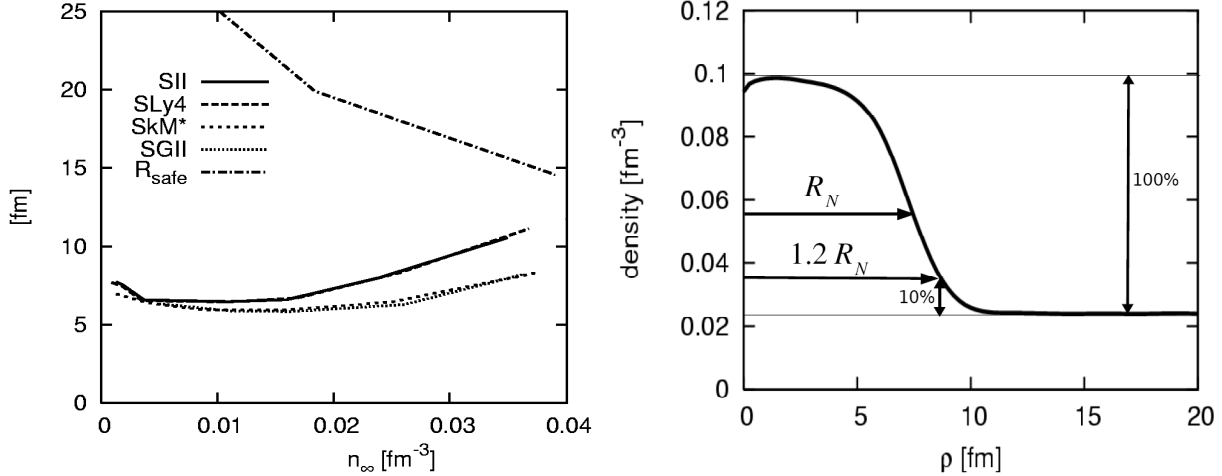


Figure 26: (left) Comparison between the vortex radius ($R_{90\%}$) and the distance R_{safe} . The interactions SII and SLy4 have very similar radii at a fixed neutron density and their curves are almost superimposed; the same is true for SkM* and SGII. (right) Illustration of the density profile obtained with the parametrization (11). At a distance $1.2 R_0$ from the center of the nucleus, the difference between the neutron density and its asymptotic value has reduced to 10% of its maximum value.

the qualitative differences in the vortex structure, discussed in the previous section.

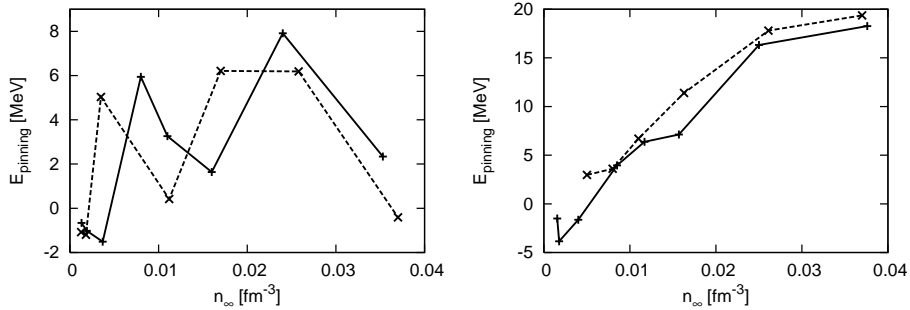


Figure 27: ((left)) Pinning energy calculated as a function of the asymptotic neutron density with the interactions SLy4 (dashed line) and SII (solid line). The lines connect the calculated points. (right) The same for the interactions SkM* (solid line) and SGII (dashed line).

SLy4 $n_{\infty}=0.001 \text{ fm}^{-3}$								
	λ	N	E_{pair}	E_{tot}	$E_{tot}+\Delta E$	E^{vor}	$E_{pinning}$	
Pinned	1.65	188.52	-103.99	-904.05	-902.68	3.37	-1.08	
Nucleus	1.6	189.35	-120.61	-906.05				
Vortex	1.65	82.09	-112.32	93.60	96.02	4.45		
Uniform	1.6	83.56	-130.98	91.57				

SLy4 $n_{\infty}=0.002 \text{ fm}^{-3}$								
	λ	N	E_{pair}	E_{tot}	$E_{tot}+\Delta E$	E^{vor}	$E_{pinning}$	
Pinned	2.05	229.87	-167.31	-825.98	-821.42	5.69	-1.20	
Nucleus	2.00	232.09	-195.74	-827.11				
Vortex	2.05	125.93	-181.19	177.47	181.11	6.89		
Uniform	2.00	127.71	-208.13	174.22				

SLy4 $n_{\infty}=0.004 \text{ fm}^{-3}$								
	λ	N	E_{pair}	E_{tot}	$E_{tot}+\Delta E$	E^{vor}	$E_{pinning}$	
Pinned	3.05	413.36	-354.79	-288.67	-288.11	19.93	5.03	
Nucleus	3.0	413.55	-447.36	-308.04				
Vortex	3.05	272.14	-407.00	567.28	576.10	14.90		
Uniform	3.0	275.03	-456.72	561.20				

SLy4 $n_\infty=0.008 \text{ fm}^{-3}$							
	λ	N	E_{pair}	E_{tot}	$E_{tot}+\Delta E$	E^{vor}	$E_{pinning}$
Pinned	4.75	783.54	-816.18	1220.08	1252.77	34.82	0.40
Nucleus	4.70	790.42	-937.12	1218.06			
Vortex	4.75	653.65	-884.15	2128.650	2148.74		
Uniform	4.70	657.88	-977.32	2114.32			

SLy4 $n_\infty=0.011 \text{ fm}^{-3}$							
	λ	N	E_{pair}	E_{tot}	$E_{tot}+\Delta E$	E^{vor}	$E_{pinning}$
Pinned	5.73	1086.7	-1068.50	2858.24	2839.90	50.09	0.42
Nucleus	5.63	1083.5	-1215.42	2789.81			
Vortex	5.74	965.4	-1146.52	3816.77	3816.77		
Uniform	5.67	962.6	-1258.76	3751.11			

SLy4 $n_\infty=0.017 \text{ fm}^{-3}$							
	λ	N	E_{pair}	E_{tot}	$E_{tot}+\Delta E$	E^{vor}	$E_{pinning}$
Pinned	7.05	1647.33	-1245.87	6544.28	6595.52	77.09	6.21
Nucleus	7.0	1654.60	-1460.55	6518.42			
Vortex	7.05	1498.32	-1375.65	7322.81	7346.86		
Uniform	7.0	1501.73	-1523.55	7275.98			

SLy4 $n_\infty = 0.026 \text{ fm}^{-3}$							
	λ	N	E_{pair}	E_{tot}	$E_{tot} + \Delta E$	E^{vor}	$E_{pinning}$
Pinned	8.55	2452.99	-1174.10	12956.57	13058.04	104.02	6.19
Nucleus	8.50	2464.86	-1467.41	12954.02			
Vortex	8.55	2301.11	-1362.87	13712.91	13714.88		
Uniform	8.50	2301.34	-1541.69	13617.05			

SLy4 $n_\infty = 0.037 \text{ fm}^{-3}$							
	λ	N	E_{pair}	E_{tot}	$E_{tot} + \Delta E$	E^{vor}	$E_{pinning}$
Pinned	10.05	3332.59	-762.77	22821.65	22814.52	122.01	-0.41
Nucleus	10.0	3332.53	-1159.46	22692.50			
Vortex	10.05	3500.58	-1012.38	23418.71	23419.28		
Uniform	10.0	3501.29	-1230.38	23296.86			

Table III: Calculation of the pinning energy with the interaction SLy4 for the various neutron densities we have considered. (cf. Table I). In each case, we give the values of the chemical potential λ , (in MeV), the number of neutrons N , the pairing energy E_{pair} (in MeV), the total energy E_{tot} (in MeV) (cf. Appendix A), associated with the four configurations labeled *Pinned* (vortex on a nucleus), *Nucleus* (nucleus in the neutron sea), *Vortex* (vortex in uniform matter), *Uniform* (uniform matter). For the configurations *Pinned* and *Vortex* we give the total energy $E_{tot} + \Delta E$ (in MeV), corrected in order to obtain the same number of neutrons as in the configurations *Nucleus* and *Uniform*. We also give the cost E^{vor} (in MeV) to create the vortex pinned on the nucleus and the vortex in uniform matter, and finally the pinning energy $E_{pinning}$ (in MeV).

SkM* $n_\infty = 0.001 \text{ fm}^{-3}$								
	λ	N	E_{pair}	E_{tot}	$E_{tot} + \Delta E$	E^{vor}	$E_{pinning}$	
Pinned	1.27	199.36	-120.64	-946.97	-938.50	3.49	-1.51	
Nucleus	1.2	206.14	-169.11	-941.99				
Vortex	1.25	89.99	-127.51	82.77	86.23	5.00		
Uniform	1.2	92.74	-149.53	81.23				

SkM* $n_\infty = 0.002 \text{ fm}^{-3}$								
	λ	N	E_{pair}	E_{tot}	$E_{tot} + \Delta E$	E^{vor}	$E_{pinning}$	
Pinned	1.40	221.48	-156.20	-917.12	-894.54	6.45	-3.85	
Nucleus	1.35	237.61	-229.53	-897.14				
Vortex	1.40	117.20	-172.05	120.66	124.78	2.61		
Uniform	1.35	120.15	-198.97	118.33				

SkM* $n_\infty = 0.004 \text{ fm}^{-3}$								
	λ	N	E_{pair}	E_{tot}	$E_{tot} + \Delta E$	E^{vor}	$E_{pinning}$	
Pinned	2.05	378.80	-413.59	-626.93	-499.45	13.70	-1.63	
Nucleus	2.00	440.98	-524.10	-513.16				
Vortex	2.05	278.08	-440.18	417.50	429.03	15.33		
Uniform	2.00	283.70	-495.26	413.70				

SkM* $n_\infty = 0.008 \text{ fm}^{-3}$							
	λ	N	E_{pair}	E_{tot}	$E_{tot} + \Delta E$	E^{vor}	$E_{pinning}$
Pinned	3.05	785.03	-919.51	459.09	512.59	39.67	3.95
Nucleus	3.00	802.57	-1085.98	472.92			
Vortex	3.05	659.10	-1002.84	1459.46	1486.87		
Uniform	3.00	668.09	-1106.10	1451.15			

SkM* $n_\infty = 0.012 \text{ fm}^{-3}$							
	λ	N	E_{pair}	E_{tot}	$E_{tot} + \Delta E$	E^{vor}	$E_{pinning}$
Pinned	3.62	1057.68	-1235.92	1420.66	1436.74	57.07	6.38
Nucleus	3.53	1062.12	-1412.41	1379.67			
Vortex	3.60	926.77	-1317.69	2401.44	2398.33		
Uniform	3.53	925.91	-1433.06	2347.63			

SkM* $n_\infty = 0.016 \text{ fm}^{-3}$							
	λ	N	E_{pair}	E_{tot}	$E_{tot} + \Delta E$	E^{vor}	$E_{pinning}$
Pinned	4.25	1397.33	-1534.87	2827.25	2970.22	73.78	7.97
Nucleus	4.20	1430.97	-1749.45	2896.34			
Vortex	4.25	1280.31	-1636.09	3864.68	3901.98		
Uniform	4.20	1289.09	-1789.18	3837.70			

SkM* $n_\infty = 0.025 \text{ fm}^{-3}$							
	λ	N	E_{pair}	E_{tot}	$E_{tot} + \Delta E$	E^{vor}	$E_{pinning}$
Pinned	5.65	2261.44	-1897.82	7286.06	7358.10	116.90	16.33
Nucleus	5.60	2274.19	-2161.68	7241.19			
Vortex	5.65	2128.52	-2026.77	8249.63	8286.71		
Uniform	5.60	2135.08	-2227.12	8186.13		100.57	

SkM* $n_\infty = 0.038 \text{ fm}^{-3}$							
	λ	N	E_{pair}	E_{tot}	$E_{tot} + \Delta E$	E^{vor}	$E_{pinning}$
Pinned	7.55	3481.75	-1857.15	15563.57	15566.52	154.43	18.27
Nucleus	7.5	3482.14	-2130.98	15412.09			
Vortex	7.55	3342.92	-1965.67	16476.96	16486.52		
Uniform	7.5	3344.18	-2210.59	16350.36		136.16	

Table IV: The same as in Table III, but for the SkM* interaction.

V. COMPARISON WITH PREVIOUS MODELS

The density dependence of the pinning energy presented above is remarkably different from that obtained in previous works.

Epstein and Baym [10] calculated the pinning energy solving the Ginzburg-Landau equation. They assumed that in the pinned configuration 'the order parameter in the nucleus would be similar to that for the unperturbed vortex line'. They calculated the kinetic energy associated with the vortex axis at a distance s from the center of the nucleus, assuming the same functional form and spatial dependence for the order parameter associated with the vortex, with or without the presence of the nucleus. Due to their basic assumption, the difference in energy between the pinned ($s = 0$) and the interstitial ($s \rightarrow \infty$) configurations only involved the condensation energy (cf. Eqs. (5.2), (A13) and (C3) of their paper). As a consequence, the pinning configuration becomes favoured when less pairing energy is suppressed by the vortex, than in uniform matter. This in turn implies, that the pairing gap inside the nucleus must be smaller than in the outer gas: this happens in their calculation for all densities larger than $10^{12.98}$ g cm $^{-3}$, or 0.0055 fm $^{-3}$.

The results obtained by Epstein and Baym are qualitatively similar to those obtained in the semiclassical model studied by Donati and Pizzochero [11] using the Argonne force, who found antipinning at low densities and pinning for densities larger than about 0.01 fm $^{-3}$ (cf. Fig. 28(c) and Fig. 33). As we discuss in Appendix C, the differences between the quantal and the semiclassical results are not due to differences in the definition of the pinning energy. In order to have some better insight, we recall that the pinning energy is the difference between the excitation energy E_{unif}^{vor} associated with a vortex created in uniform matter and the excitation energy E_{nuc}^{vor} associated with a vortex built on the nuclear volume (cf. Eq. (9)). In the model of ref. [11] these excitation energies result from two essential contributions. One of them is the condensation energy E_{cond} , associated with the pairing fields calculated with and without the presence of the vortex. The other is the kinetic energy E_{flow} associated with the velocity field created by the vortex. For each of the four relevant configuration (pinned, nucleus, vortex, uniform), E_{flow} and E_{cond} are obtained integrating respectively the kinetic energy density $1/2 \Phi^2/n$, and the condensation energy density $-3/8 [n(\rho, z)\Delta^2(\rho, z)/(\lambda - U^{HF}(\rho, z))]$. The excitation energy associated with the pinned vortex is estimated as $E_{nuc}^{vor} = [E_{flow} + E_{cond}]_{pinned} - [E_{flow} + E_{cond}]_{nucleus}$. Similarly,

$E_{unif}^{vor} = [E_{flow} + E_{cond}]_{vortex} - [E_{flow} + E_{cond}]_{uniform}$. Finally, the pinning energy is obtained as $E_{pinning} = E_{nuc}^{vor} - E_{unif}^{vor}$. The contribution of E_{flow} to the pinning energy is then $E_{flow} \equiv [E_{flow}]_{pinned} - [E_{flow}]_{nucleus} - [E_{flow}]_{vortex} + [E_{flow}]_{uniform}$, and similarly for E_{cond} . The values of E_{flow} and E_{cond} obtained in the semiclassical model of Ref.[11] are shown in Fig. 28(c) as a function of density. It is seen that E_{cond} is negative for densities larger than about 0.01 fm^{-3} . This is associated with the fact that the pairing gap in the nucleus is smaller than in the external neutron gas. Consequently, creating a vortex passing through the nucleus destroys less pairing energy than creating a vortex in uniform matter. The gain in condensation energy is largest, when the pairing gap in the neutron gas is maximum ($k_F \sim 0.8 \text{ fm}^{-1}$, or $n \sim 0.02 \text{ fm}^{-3}$, cf. Fig. 3). The radius of the vortex core is 2-3 fm larger in the pinned than in the uniform case (cf. Fig. 29); this leads to a modest reduction of the kinetic energy in the pinned case. As a consequence the contribution of E_{flow} is negative and rather small.

In the semiclassical model, the radius of the vortex core is determined requiring that the absolute value of the condensation energy density be equal to the value of the kinetic energy density associated with the vortex flow. In uniform matter the vortex core is equal to the coherence length ξ which is of the order, or larger than the nuclear radius R_0 . At high neutron densities in the crust $\xi > R_0$; the nucleus is included in the vortex core and cannot influence its properties. The semiclassical model is then very similar to Epstein and Baym's and the pinning energy is only due to the contribution from the condensation energy (cf. Fig. 28(c)). At lower neutron density, $\xi \sim R_0$. In this case the kinetic energy density increases on the nuclear surface leading to an increase of the core radius of 2-3 fm. In this case the pinning energy receives a contribution also from the kinetic energy.

In Fig. 28(a) and (b) we show the quantities E_{flow} and E_{cond} obtained from our calculated potentials, pairing gaps, currents and densities associated with the SLy4 and SkM* mean fields. For densities lower than about 0.02 fm^{-3} , the results obtained with the two mean fields are rather similar, and are substantially different from the semiclassical results: both E_{flow} and E_{cond} are much larger in absolute value and E_{cond} takes positive values. This difference is directly related to the much larger vortex radius we calculated in the pinned configuration (cf. Fig.25). In turn, this is associated with shell effects, which have been discussed above in Sec. IV and which are not considered in the semiclassical model, As a consequence, in our calculations pairing is suppressed not only inside the nuclear volume, but also in a large layer (6-7 fm thick) in the interface region between the nuclear surface

and the neutron gas (cf. Fig. 15). This changes the energy balance as compared to the semiclassical model, and makes it less favourable to build the vortex on the nucleus. One should also add that, due to proximity effects, the pairing field does not vanish in the nuclear volume, as it happens in the Local Density Approximation with the Argonne potential (cf. Fig. 8-10) [27]. On the other hand, the large core radius implies the suppression of the velocity field in a large volume (cf. Fig. 16), leading to large negative values of E_{flow} .

At densities larger than about 0.02 fm^{-3} , one can notice a change in the density dependence of E_{flow} and E_{cond} in the case of the SkM* interaction: E_{flow} increases and E_{cond} decreases, reaching values closer to the semiclassical ones. This is related to the weakening of shell effects for $\lambda > 10 \text{ MeV}$ with this interaction (cf. Fig. 22).

While in the semiclassical model the pinning energy is essentially the sum of E_{flow} and E_{cond} , in our self-consistent calculations, the changes in the mean field induced by the vortex play an important role. This can be seen in Figs. 28(a),(b), where we compare the pinning energy with the sum $E_{flow} + E_{cond}$. The contributions of the changes in the mean field to the pinning energy are of the order of 5-10 MeV: they are smaller than the range of values of E_{flow} or E_{cond} but are relevant for a quantitative assessment of the pinning energy, leading in some cases to a change of its sign.

VI. CONCLUSIONS

Vortices are one of the clearest examples of the quantal nature of superfluids. In particular of Fermi superfluids made out of a large number of overlapping Cooper pairs. Rotation can only happen by giving one ($\nu = 1$) or more ($\nu = 2, \dots$) units of angular momentum to each Cooper pair. It is then not surprising that the properties of these rotonic excitations in a rather complex many-body system like that of finite nuclei forming a Coulomb lattice immersed in a sea of free neutrons display a complex dynamics, reflecting simultaneously the variety of quantal behaviour associated with both finite and infinite systems. In particular spatial quantization typical of finite many-body systems which provides special bunchiness to the single-particle levels and is responsible not only for the special stability of certain nuclear species, but also determines the structure of single-particle resonances in the continuum: nuclear structure and nuclear reaction aspects of the same phenomenon.

The effective mass (m_k) associated with the nucleon-nucleon interactions used to describe

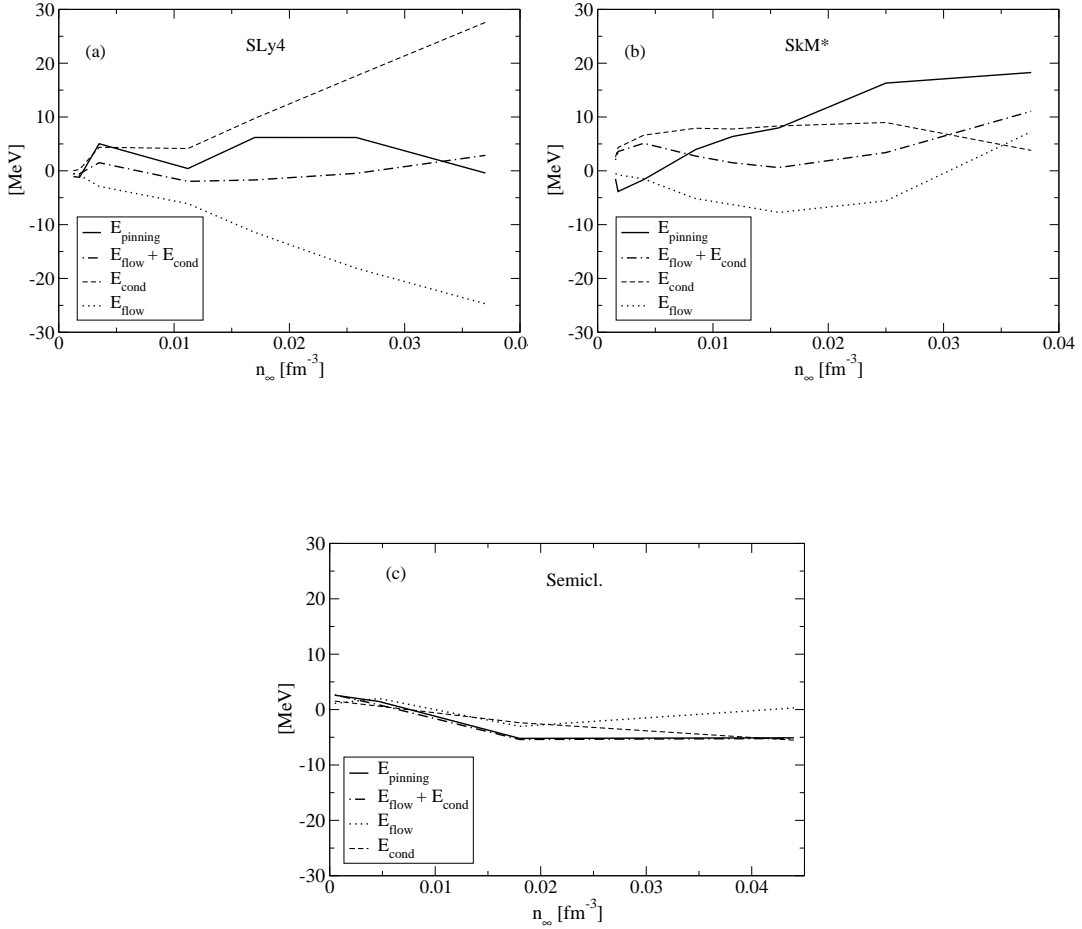


Figure 28: Pinning energy, flow energy and condensation energy (in MeV) derived from the HFB calculations using the SLy4 mean field (a) or the SkM* mean field (b). In (c) we show the same quantities calculated in the semiclassical model.

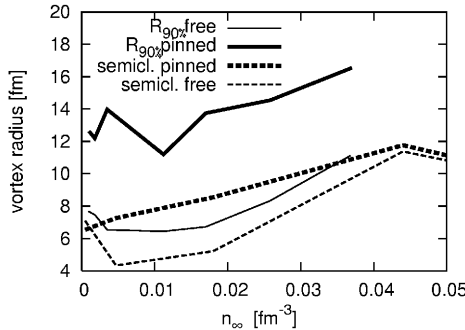


Figure 29: The radii of the free and pinned vortex according to our quantal model (cf. Fig. 25) calculated with the SLy4 and with the SkM* mean fields are compared with the radii obtained in the semiclassical model of ref. [11]

the system makes these effects more or less important depending on whether m_k is smaller than, or close to the bare mass m , in keeping with the fact that the associated mean fields are deeper or shallower, leading to larger or smaller energy separations between resonances of different parities, respectively.

While the associated results for the pinning energy are quite different, in the first case ($m_k < m$) producing a bell shape like pinning energy behaviour as a function of density, and in the second case ($m_k \sim m$) predicting a linearly increasing behaviour, both are quite different from the semiclassical result. Consequently, while we cannot say which of the two behaviours is correct due to the existing latitude in the parametrization of effective nuclear forces, one can conclude that there is likely no alternative to a full quantal treatment of the nucleus-vortex interaction in the determination of the pinning energies. To become quantitative, one needs to consider on par with the bare nucleon-nucleon interaction, the induced interaction arising from the exchange of density and spin modes, taking into account both self-energy, vertex and induced interaction type of processes. There is a formidable task lying ahead, if one wants to become quantitative and realistic concerning the vortex-nucleus interaction in the situation typical of the inner crust of a neutron star. We believe that one can attack this problem with good chances of success capitalizing on the results obtained in the present work.

VII. APPENDIX A

The HFB equations can be written in cylindrical coordinates as

$$\begin{aligned} (\hat{T} + U^{HF}(\rho, z) - \lambda)u_{qm}(\rho, z, \phi) + \Delta(\rho, z, \phi)v_{qm}(\rho, z, \phi) &= E_{qm}u_{qm}(\rho, z, \phi) \\ \Delta^*(\rho, \phi, z)u_{qm}(\rho, z, \phi) - (\hat{T} + U^{HF}(\rho, z) - \lambda)v_{qm}(\rho, z, \phi) &= E_{qm}v_{qm}(\rho, z, \phi). \end{aligned} \quad (13)$$

The kinetic energy operator, $\hat{T} = -\frac{\hbar^2}{2}\nabla \frac{1}{\mu(\rho, z)}\nabla$ contains the effective mass $\mu(\rho, z)$ associated with the adopted Skyrme interaction, while Δ is the pairing field and U^{HF} is the mean field potential calculated using the Skyrme functional. We include all the terms of the Skyrme functional listed in Eqs.(2.1) of ref. [23], except for the spin-orbit and the spin gradient terms. The index q labels the different quasiparticle energies E and amplitudes u, v associated with a projection m of the orbital angular momentum along the z -axis. Since we neglect the spin-orbit interaction, the spin degree of freedom is taken into account simply by the degeneracy factor $g = 2$.

For a system with axial symmetry respect to the z -axis, the characteristic ansatz for the study of the vortex is [20, 24, 25]

$$\Delta(\rho, z, \phi) = \Delta(\rho, z)e^{i\nu\phi}, \quad (14)$$

where $\nu = 0, 1, 2\dots$ is the vortex index.

The normal and abnormal densities are given by

$$n(\rho, z, \phi) = 2 \sum_{qm} v_{qm}(\rho, z, \phi)v_{qm}^*(\rho, z, \phi) \quad (15)$$

and by

$$\kappa(\rho, z, \phi) = \sum_{qm} u_{qm}(\rho, z, \phi)v_{qm}^*(\rho, z, \phi), \quad (16)$$

and the gap is given by

$$\Delta(\rho, z, \phi) = -V_{pair}\kappa(\rho, z, \phi). \quad (17)$$

The Hartree-Fock field U^{HF} is calculated according to Eq. (2.8) of ref. [23]. We assume the following form for the dependence of the quasiparticle amplitudes on the angle ϕ :

$$\begin{aligned} u_{qm}(\rho, z, \phi) &\sim e^{im\phi} & ; \\ v_{qm}(\rho, z, \phi) &\sim e^{i(m-\nu)\phi}. \end{aligned} \quad (18)$$

In this way, Eqs.(16) and (17) lead to a pairing field which is consistent with the ansatz (14).

We shall only solve the axially symmetric equation for the neutrons. According to the study of Negele and Vautherin [1], who neglected pairing in the minimization of their energy functional, the favoured number of protons is mostly determined by shell effects, and varies from $Z = 40$ to $Z = 50$. Because we neglect the spin-orbit interaction, the natural choice for us is to assume $Z = 40$, corresponding to a shell closure. However, more recent studies including pairing have shown that the value of Z can depend on the details of the functional, being sometimes rather different from Negele and Vautherin's solution [18]. We have not investigated whether a different choice of Z would lead to important changes in our results. The protons are deeply bound and for this reason they are not expected to be influenced significantly by the vortex, and thus the proton field should essentially keep spherical symmetry. We then perform a simple spherical HF calculation for the protons, enclosing them in a spherical box of radius 15 fm, and carry out a spherical average of the neutron part of the potential felt by the protons (in particular at each iteration we replace the neutron density $n(\rho, z)$ by an isotropic $n_{av}(r)$ obtained averaging $n(\rho, z)$ on the surface of a sphere of radius r).

We shall solve the HFB equations in a cylindrical cell of radius ρ_{box} and height h_{box} (cf. Fig. 4), imposing the boundary condition $u_{qm}(\rho, z, \phi) = v_{qm}(\rho, z, \phi) = 0$ for $\rho = \rho_{box}$, or $z = \pm h_{box}/2$. We shall expand the quasiparticle amplitudes on a single-particle basis writing

$$\begin{aligned} u_{qm}(\rho, z, \phi) &= \sum_{ih} U_{hi;qm} \phi_{hm}(\rho) \psi_i(z) e^{im\phi} \\ v_{qm}(\rho, z, \phi) &= \sum_{ih} V_{hi;qm} \phi_{h(m-\nu)}(\rho) \psi_i(z) e^{i(m-\nu)\phi}. \end{aligned} \quad (19)$$

In the z -direction we have taken the set of standing waves

$$\psi_i(z) = \sqrt{\frac{2}{h_{box}}} \sin(k_i(z + h_{box}/2)), \quad k_i = \frac{\pi}{h_{box}}, \frac{2\pi}{h_{box}}, \dots \quad (20)$$

In the ρ direction we have taken the set of solutions associated with the Schrödinger equation for free neutrons:

$$\left[-\frac{\hbar^2}{2\mu_0} \frac{1}{\rho} \frac{d}{d\rho} \rho \frac{d}{d\rho} + \frac{\hbar^2 m^2}{2\mu_0 \rho^2} \right] \phi_{hm}(\rho) = \epsilon_{hm} \phi_{hm}(\rho), \quad (21)$$

where μ_0 indicates the bare nucleon mass. Projecting the HFB equations on the chosen single-particle basis, we obtain two algebraic equations for the expansion coefficients

$U_{hi;qm}, V_{hi;qm}$:

$$\begin{aligned} \sum_{hi} (K_{lhij,m} - \lambda) U_{hi;qm} + \sum_{hi} U_{lhij,m}^{HF} U_{hi;qm} + \sum_{hi} \Delta_{lhij,m} V_{hi;qm} &= E_{qm} U_{lj;qm} \\ \sum_{hi} \Delta_{lhij,m} U_{hi;qm} - \sum_{hi} (K_{lhij,m-\nu} - \lambda) V_{hi;qm} - \sum_{hi} U_{lhij,m-\nu}^{HF} V_{hi;qm} &= E_{qm} V_{lj;qm}. \end{aligned} \quad (22)$$

The matrix elements of the kinetic energy, of the mean field and of the pairing field are given by

$$K_{lhij,m} = 2\pi \int d\rho dz \rho \phi_{lm}(\rho) \psi_j(z) \left[\left(\frac{\mu_0}{\mu(\rho, z)} \epsilon_{lm} + \frac{\hbar^2 k_j^2}{2\mu(\rho, z)} \right) - \frac{\hbar^2}{2} (\nabla \frac{1}{\mu(\rho, z)}) \cdot \nabla \right] \phi_{hm}(\rho) \psi_i(z); \quad (23)$$

$$U_{lhij,m}^{HF} = 2\pi \int d\rho dz \rho \phi_{lm}(\rho) \psi_j(z) U^{HF}(\rho, z) \phi_{hm} \psi_i(z); \quad (24)$$

$$\Delta_{lhij,m} = 2\pi \int d\rho dz \rho \phi_{lm}(\rho) \psi_j(z) \Delta(\rho, z) \phi_{h(m-\nu)} \psi_i(z). \quad (25)$$

The total energy is given by $E_{tot} = E_{HF} + E_{pair}$, where E_{HF} calculated according to Eq. (2.2) of ref. [23] and E_{pair} is obtained by

$$E_{pair} = -\frac{1}{2} \int d\rho dz d\phi \rho \kappa^*(\rho, z, \phi) \Delta(\rho, z, \phi) \quad (26)$$

In the literature, one finds different choices concerning the boundary conditions applied to calculations in Wigner-Seitz cells. In Fig. 30 we compare the values of the gap at the Fermi energy Δ_F obtained with the SLy4 mean field as a function of the Fermi momentum in a spherical box of radius $R = 30$ fm, with those independently calculated in infinite neutron matter and already shown in Fig. 3. We have used three different boundary conditions for the single-particle wavefunctions: (a) all the wavefunctions vanish at the edge of the cell (the boundary condition adopted in this paper) (b) the wavefunctions of even orbital angular momentum and the derivatives of the wavefunctions of odd orbital angular momentum vanish at the edge of the cell (the boundary condition adopted by Negele and Vautherin); (c) the same as (b), but exchanging the role of odd and even angular momenta. It is seen that the agreement with the result obtained in infinite matter is of the same quality in the three cases (cf. also the discussion in ref. [28]).

We have also checked that with our boundary conditions (a) we reproduce accurately the values of the energy per particle in neutron matter calculated analytically with the Skyrme interactions we have considered. As we discussed in Section IVB, using boundary conditions (a) we have also been able to reproduce the pairing gap associated with the vortex ($\nu = 1$), calculated by Bulgac and Yu in infinite neutron matter.

For calculations with protons, that is, with a nucleus at the center of the box, we have found that in all the calculations reported in this paper, the pairing gap at large distances ($\rho > 20$ fm) resumes the value calculated in uniform neutron matter at the relevant density. Obviously with boundary conditions (a) the pairing gap drop quickly to zero at the edge of the box. We have checked that this does not influence the calculations of the pinning energy, which is obtained subtracting the energies of different configurations, as discussed in the next Section.

In all our calculations we have used boxes with radii equal to, or larger than, 30 fm. In other works, where one has to calculate the pairing gap inside the actual Wigner-Seitz cells, one finds some clear dependence on the boundary condition for cells smaller than about 20 fm [18]. In this case, one should consider in detail the influence of the Coulomb lattice [5].

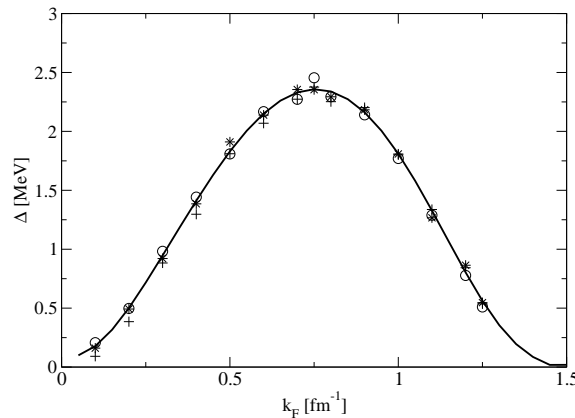


Figure 30: Comparison between the gap obtained requiring that the radial single-particle wave-functions $u_L(r)$ vanish at the edge of the spherical box for all orbital angular momenta L (crosses), or that $u_L(R)$ (for L even) and du_L/dR (L odd) vanish at the edge of the box (stars), or that $u_L(R)$ (for L odd) and du_L/dR (L even) vanish at the edge of the box (circles). The solid curve shows the pairing gap calculated in infinite neutron matter.

VIII. APPENDIX B

In this Appendix we give some details concerning the numerical accuracy of the calculation of the pinning energy. This is important, because the pinning energy, which is of the

order of a few MeV, results from the difference of the total energies of the various configurations, which are of the order of a few GeV. The main parameter that influence the accuracy of our calculation is the mesh size. Furthermore, we have to check that the size of the box (that is, its height h_{box} and its radius ρ_{box}) is sufficiently large, to obtain stable results. As we discussed in Section IVC, we expect that values like $h_{box} = 40$ fm and $\rho_{box} = 30$ fm are sufficiently large to guarantee that the pinning process is not significantly influenced by the boundary. In fact, the typical vortex radius, as measured by $R_{90\%}$, is about 15 fm (cf. Fig. 25). Moreover, the calculation of the pinning energy is more sensitive to the value of ρ_{box} than to h_{box} , because the distortion of the pinned vortex is much more relevant on the equator (cf. for example Fig. 14). We have studied in a few cases the dependence of the computed values of the pinning energy on ρ_{box} , making calculations of the relevant configurations with different boxes. In Tab. V and in Tab. VI we show the values of the pinning energy calculated with different box sizes for the SII and SLy4 interactions. The values show very modest fluctuations with the box size for the points associated with densities up to about $n < 0.017 \text{ fm}^{-3}$, for which we can estimate an uncertainty of the order of 200 keV. For the highest density points, the fluctuations become larger, but do not exceed 1-2 MeV. This is related to the fact that the vortex radius increases with density, particularly with the SII and SLy4 interactions (cf. Fig. 25).

λ [MeV]	n_∞ [fm^{-3}]	$\rho_{box} = 30$ fm	$\rho_{box} = 25$ fm
3	0.004	-1.51	-1.65
5.8	0.011	3.26	3.46
7	0.016	1.64	1.34
11.3	0.035	2.34	1.77

Table V: Pinning energy (in MeV) calculated with the SII interaction at various values of the chemical potential and of the asymptotic neutron densities, for two different radii of the cylindrical box.

The size of the mesh in ρ and z used in the code that solves the HFB equations and calculates the energy is crucial for the accuracy of the calculations. We have studied the influence of the mesh (for the ρ coordinate) in the case of the SLy4 interaction at the density

λ [MeV]	n_∞ [fm $^{-3}$]	$\rho_{box} = 35$ fm	$\rho_{box} = 30$ fm	$\rho_{box} = 25$ fm
5.7	0.011	0.45	0.42	-0.3
7	0.017	6.07	6.21	5.54
10	0.037	1.64	-0.41	1.78

Table VI: Pinning energy (in MeV) calculated with the SLy4 interaction at various values of the chemical potential and of the asymptotic neutron densities, for three different radii of the cylindrical box.

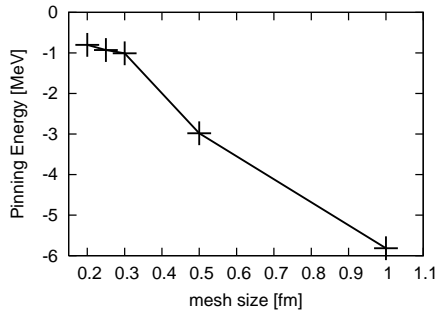


Figure 31: Pinning energy calculated with the SLy4 interaction at the density $n_\infty = 0.001$ fm $^{-3}$ as a function of the mesh size used in the ρ -coordinate.

$n_\infty = 0.0013$ fm $^{-3}$ and the results are shown in Fig. 31. The fluctuations of the pinning energy for a mesh smaller than 0.3 MeV are of the order of hundreds of keV ($\lesssim 0.2$ MeV).

IX. APPENDIX C

In a semiclassical study of the problem under discussion [11] the pinning energy was defined as the difference of the energies associated with the pinned and the interstitial configurations, taking explicitly into account the presence of one of the neighbouring nuclei (cf. the left part of Fig. 32). This definition of pinning energy reduces to ours, if the interaction of the vortex with the second nucleus is negligible. We have tested the importance of the neighboring nucleus within the semiclassical model, for the range of densities we have considered. We first computed the energy of each of the relevant configurations using the semiclassical theory, the two pairing interactions (Argonne and Gogny) and the parameters

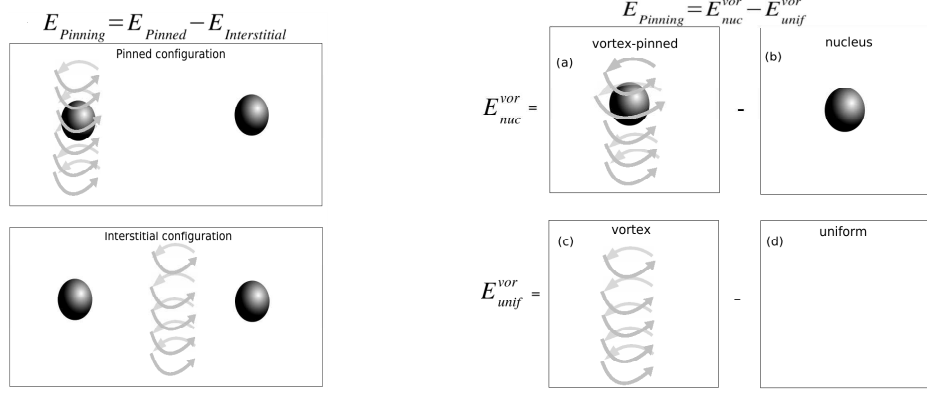


Figure 32: (left) The scheme used by Donati and Pizzochero [11] where the pinning energy takes into account the presence of a neighboring nucleus; (right) the scheme we used, where the pinning energy is evaluated as the difference between the costs to excite a vortex on a nucleus and in uniform matter.

presented in Ref. [11], instead of solving the HFB equations. We then calculated the pinning energy using the scheme proposed in Ref. [11]: the resulting values are connected by the dashed curves in Fig. 33, and they reproduce quite accurately the values reported in ref. [11], already shown in Fig. 28(c) in the case of the Argonne interaction. In Fig. 33 we also show the pinning energies calculated using the semiclassical energies, but using our scheme (cf. the right part of Fig. 32). The two schemes yield an almost equal result, showing that the differences existing between the quantal and the semiclassical calculations are not due to the geometrical scheme used to derive the pinning energy, and that the contribution of the second nucleus plays in fact a marginal role, also following the formalism of ref. [11]. The situation may change at larger densities, where the vortex radius becomes of the order of the internuclear distance, as we have discussed in Section IV C.

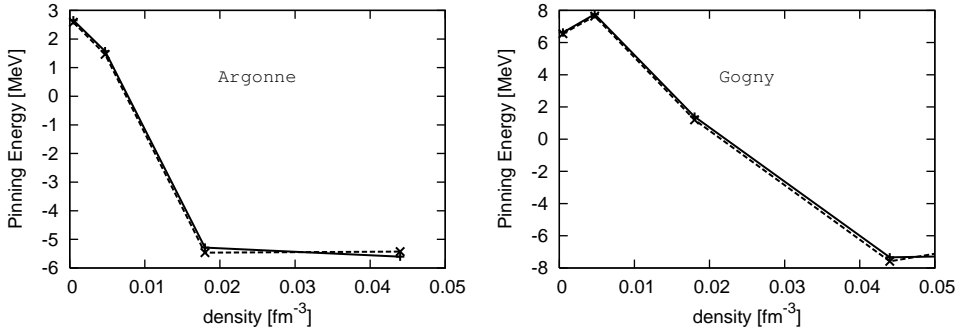


Figure 33: Solid and dashed curves show respectively the pinning energies calculated using our scheme (Fig. 5, right part), or the scheme of Ref.[11] (Fig. 5, left part). In both cases, we have computed the energies of the different configurations using the semiclassical model, with the Argonne pairing interaction (left panel) or the Gogny pairing interaction (right panel).

-
- [1] J.W. Negele and D. Vautherin, Nucl. Phys. **A207** (1973) 298.
- [2] C.J. Pethick and D.G. Ravenhall, Annu. Rev. Nucl. Part. Sci. **45** (1995) 429.
- [3] C.J. Horowitz, M.A. Perez-Garcia, D.K. Berry and J. Piekarewicz, Phys. Rev. **C72** (2005) 035801.
- [4] G. Watanabe, T. Maruyama, K. Sato, K. Yasuoka and T. Ebisuzaki, Phys. Rev. Lett. **94** (2005) 031101.
- [5] N. Chamel, S. Naimi, E. Khan, J. Margueron, Phys. Rev. **C75** (2007) 55806.
- [6] U. Lombardo and H.-J. Schulze, in *Physics of neutron star interiors*, D. Blaschke, N.K. Glendenning and A. Sedrakian eds., Springer-Verlag (2001), p. 30, and refs. therein.
- [7] P.W. Anderson and N. Itoh, Nature **256** (1975) 25.
- [8] B. Link, R.I. Epstein and G. Baym, Astrophys. J. **403**(1993)285; M. B. Larson and B. Link, Mon. Not. R. Astron. Soc. **333**(2001)613; B. Link and C. Cutler, Mon. Not. R. Astron. Soc. **336**(2002)211; M. Hirasawa and N. Shibasaki, Astrophys. J. **563**(2001)267; P.B. Jones, Phys. Rev. Lett. **79**(1997)792; **81**(1998)4560; Mon. Not. R. Astron. Soc. **257**(1998)501; **296**(1998)217.
- [9] B. Link, R.I. Epstein, and J.M. Lattimer, Phys. Rev. Lett. **83** (1999) 3362.
- [10] R.I. Epstein and G. Baym, Astrophys. J. **328** (1988) 680.
- [11] P. Donati and P.M. Pizzochero, Nucl. Phys. **A742** (2004)363 .
- [12] P. Donati and P.M. Pizzochero. Phys. Lett. **B640** (2006)74.
- [13] A. Bulgac and Y. Yu, Phys. Rev. Lett. **90** (2003)161101.
- [14] P. Avogadro, F. Barranco, R.A. Broglia, and E. Vigezzi, Phys. Rev. **C75** (2007) 012805(R).
- [15] P. Avogadro, F. Barranco, R.A. Broglia and E. Vigezzi, in *Exotic states of nuclear matter*, eds. U. Lombardo, M. Baldo, F. Burgio and H.-J. Schulze, World Scientific (2008), p. 396.
- [16] P. Avogadro, F. Barranco, R.A. Broglia and E. Vigezzi, Nucl. Phys. **A788** (2007) 130c.
- [17] G. Gori, F. Ramponi, F. Barranco. R.A. Broglia, G. Coló, D. Sarchi and E. Vigezzi, Nucl. Phys. **A731** (2004) 401.
- [18] M. Baldo, U. Lombardo, E.E. Saperstein and S.V. Tolokonnikov, Nucl. Phys. **A750** (2005) 409; M. Baldo, E.E. Saperstein and S.V. Tolokonnikov, Nucl. Phys. **A775** (2006) 235.
- [19] P. Ring and P. Schuck, *The nuclear many body problem*, Springer Verlag (1980).

- [20] P.G. de Gennes, *Superconductivity in metals and alloys*, Benjamin (1996).
- [21] M. Baldo, C. Maieron, P. Schuck, and X. Viñas, Nucl. Phys. **736** (2004) 241.
- [22] E. Garrido, P. Sarriuguren, E. Moya de Guerra, and P. Schuck, Phys. Rev. **C60** (1999) 064312.
- [23] E. Chabanat, P. Bonche, P. Haensel, J. Meyer and R. Schaeffer, Nucl. Phys. **A635** (1998) 213.
- [24] A. Bohr and B.R. Mottelson, Phys. Rev. **125** (1962) 495.
- [25] F. Gygi and M. Schlüter, Phys. Rev. **B43**(1991) 7609.
- [26] Y.M. Engel, D.M. Brink, K. Goeke, S.J. Krieger and D. Vautherin, Nucl. Phys. **A249** (1975) 215.
- [27] P.M. Pizzochero, F. Barranco, R.A. Broglia and E. Vigezzi, Astrophys. J. **569** (2002) 381.
- [28] F. Montani, C. May and H. Müther, Phys. Rev. **C69** (2004) 065801.
- [29] N. Sandulescu, Phys. Rev. **C70** (2004) 025801; N. Sandulescu, N. Van Giai and R.J. Liotta, Phys. Rev. **C69** (2004) 045802.
- [30] Ø. Elgarøy and F. De Blasio, Astr. & Astroph. **370** (2001) 939.
- [31] B. Link, Phys. Rev. Lett. **91** (2003) 101101-1.